NTNU

Norwegian University of
Science and Technology

Motion Tracking by Transverse Oscillations in 3D Cardiac Ultrasound Imaging

Solveig Bech

Master of Science in Cybernetics and Robotics
Submission date: June 2017
Supervisor: Hans Torp, ITK
Co-supervisor: Sebastien Salles, Institutt for sirkulasjon og bildediagnostikk

Norwegian University of Science and Technology
Department of Engineering Cybernetics

Problem Description

Motion tracking in dynamic 3D ultrasound images is an important tool for the clinician to evaluate heart function for several severe cardiac diseases, including myocardial infarction and angina. Block matching techniques have limited performance due to poor lateral resolution and low frame rate. At NTNU we have developed a new 3D data acquisition technique with very high frame rate (500-1000 frames/sec). This makes it possible to use a Doppler technique referred to as transverse oscillations to obtain displacement estimates in all three dimensions. The method can be implemented in the spatial Fourier domain. Three different filtering schemes for introduction of transverse oscillations should be developed and implemented in Matlab. The first filtering method will be based on the work done by Jensen's research group [1], the second approach will be based on publications by Salles et al [2]., while the third will be a novel approach that uses three subapertures instead of four. The methods should be tested and compared to block matching by performing phantom experiments with known motion, and preferably also tested *in vivo* of a human heart.

[1] M. J. Pihl and J. A. Jensen. 3D vector velocity estimation using a 2D phased array. In 2011 IEEE International Ultrasonics Symposium, pages 430–433, 2011
[2] S. Salles, H. Liebgott, D. Garcia, and D. Vray. Full 3-D transverse oscillations: a method for tissue motion estimation. IEEE Transactions on Ultrasonics, Ferro-electrics, and Frequency Control, 62(8):1473–1485, 2015

Abstract

Quantitative measurements of myocardial deformation has proved to be useful in assessment of cardiovascular diseases. Therefore, estimation of the motion of cardiac tissue has been an active field of research for many years. Tissue Doppler imaging is a technique widely used in clinical practice to estimate tissue motion. However, this method is only able to estimate the 1D motion along the beam axis. Several methods for 2D and 3D motion estimation of tissue have been proposed. In this thesis, four procedures for 3D motion estimation of tissue have been developed in Matlab and compared in terms of accuracy and computational efficiency. Three of the estimators are based on transverse oscillations to estimate the 3D motion, and exploits three different approaches for filtering the spatial frequency content of the images. The fourth method is a speckle tracking approach based on block matching. The first filtering approach is based on work done by Jensen's research group, and filters the spatial frequency content to introduce transverse oscillations in each transverse direction separately. The second method is based on filtering the spatial frequency content to keep four separate ranges of frequency in order to introduce transverse oscillations in both transverse directions simultaneously. The third filtering approach is a novel approach that proposes to filter the spatial frequency content to keep only three separate ranges of frequency.

Phantom experiments with known motion either along a straight line or along a circular path were used for validation of the four methods. The motion estimation approaches were also tested on an *in vivo* example from the heart of a healthy volunteer. The transverse oscillation method based on filtering the spatial frequency content of the ultrasound images to keep three separate ranges of frequency, yielded the most accurate estimates of the z- and y-component of the circular velocity, with mean errors of 0.0062 mm/frame ± 0.0031 mm/frame and 0.0107 mm/frame ± 0.0085 mm/frame, respectively. The transverse oscillations approach based on the work done by Jensen's research group, yielded the most accurate estimate of the x-component of the circular motion with mean error of 0.0032 mm/frame ± 0.0025 mm/frame. On the other hand, block matching yielded significantly poorer estimates in the transverse directions than any of the methods based on transverse oscillations. Motion estimation based on block matching resulted in mean errors of 0.0071 mm/frame ± 0.0036 mm/frame in the z-direction, 0.0494 mm/frame ± 0.0255 mm/frame in the x-direction and 0.0396 mm/frame ± 0.0206 mm/frame in the y-direction. Results from this thesis have been submitted and accepted for oral presentation at the IUS 2017 conference.

Sammendrag

Kvantitative målinger av deformasjon i myokardet har vist seg å være nyttig for å evaluere kardiovaskulære sykdommer. Derfor har estimering av hjertevevets bevegelse vært et aktivt felt innenfor forskning i mange år. Vevsdoppler er en teknikk som er mye brukt i klinisk praksis for å estimere vevets bevegelse. Utfordringen med denne metoden er at den bare kan estimere 1D bevegelse langs stråleaksen for de utsendte ultralydpulsene. Flere tilnærminger har blitt foreslått for å estimere 2D og 3D vevsbevegelse. I denne oppgaven har fire metoder for å estimere den tredimensjonale vevsbevegelsen blitt utviklet og sammenlignet i forhold til nøyaktighet og kjøretid. Tre av disse estimatorene er basert på bruk av transversale oscillasjoner for å estimere 3D bevegelse, og benytter tre ulike måter å filtrere det romlige frekvensinnholdet i bildene på. Den fjerde metoden er en "speckle tracking"-tilnærming basert på "block matching". Den første filtreringsmetoden er basert på arbeid gjort av Jensens forskningsgruppe, og filtrerer det romlige frekvensinnholdet for å introdusere transversale oscillasjoner i hver tverrgående retning for seg. Den andre metoden er basert på å filtrere det romlige frekvensinnholdet slik at fire separate frekvensområder beholdes for å introdusere transversale oscillasjoner i begge tverrgående retninger samtidig. Den tredje filtreringsmetoden er en ny tilnærming som foreslår å filtrere det romlige frekvensinnholdet slik at kun tre separate frekvensområder beholdes.

Fantomeksperimenter med kjent rettlinjet eller sirkulær bevegelse ble brukt for å validere de fire metodene. Bevegelsesestimatorene ble også testet på et *in vivo* eksempel fra hjertet til en frisk frivillig. Metoden som baserer seg på å filtrere det romlige frekvensinnholdet til ultralydbilder slik at kun tre separate frekvensområder beholdes, ga mest nøyaktige estimater av z- og y-komponentene av hastigheten i den sirkulære bevegelsen, med gjennomsnittlige feil på henholdsvis 0.0062 mm/frame ± 0.0031 mm/frame og 0.0107 mm/frame ± 0.0085 mm/frame. Bevegelsesestimatoren som er basert på arbeidet gjort av Jensens forskningsgruppe, ga det mest nøyaktige estimatet av x-komponenten av hastigheten i den sirkulære bevegelsen, med en gjennomsnittlig feil på 0.0032 mm/frame ± 0.0025 mm/frame. På den andre siden ga "block matching" vesentlig dårligere estimater av de tverrgående hastighetskomponentene enn noen av metodene som baserer seg på transversale oscillasjoner. Estimering av bevegelsen ved bruk av "block matching" resulterte i gjennomsnittlige feil på 0.0071 mm/frame ± 0.0036 mm/frame i z-retning, 0.0494 mm/frame ± 0.0255 mm/frame i x-retning og 0.0396 mm/frame ± 0.0206 mm/frame i y-retning. Resultater fra denne oppgaven har blitt sendt inn og godtatt for muntlig presentasjon på konferansen IUS 2017.

Preface

This master thesis has been written in fulfillment of the requirements for the Master of Science in Cybernetics and Robotics at the Norwegian University of Science and Technology. The work was carried out during the spring of 2017, and has been conducted in collaboration with the Department of Circulation and Medical Imaging.

I would like to thank my supervisor Hans Torp for useful input and guidance throughout the semester, for sharing his knowledge on the field of ultrasound and for valuable feedback on the report. Also, I would like to thank my co-supervisor Sebastien Salles for guidance, help with experiment setups and the *in vivo* results. Finally, I would like to thank my family for the support and encouragements they have given me. A special thanks to Kjell Ragnar Løvåsen for proofreading and Ole André Bech for daily support.

Trondheim, June 2017
Solveig Bech

Contents

Nomenclature

Acronyms

BM Block Matching

FWHM Full Width Half Maximum

NCC Normalized Cross Correlation

PRF Pulse Repetition Frequency

PW Pulsed Wave

RF Radio Frequency

ROI Region Of Interest

SAD Sum of Absolute Differences

SNR Signal to Noise Ratio

SSD Sum of Squared Differences

TDI Tissue Doppler Imaging

TO Transverse Oscillation

Symbols

σ_x Width of the Gaussian function used to introduce the transverse oscillations in azimuth direction

σ_y Width of the Gaussian function used to introduce the transverse oscillations in elevation direction

c Speed of sound

f_ϕ Spatial frequency in the elevation direction

f_θ Spatial frequency in the azimuth direction

f_r Spatial frequency in the axial direction

f_{0x} Frequency of the introduced transverse oscillations in azimuth direction

f_{0y} Frequency of the introduced transverse oscillations in elevation direction

f_0 Center frequency of the ultrasound system

1 Introduction

Cardiovascular diseases are the leading cause of death worldwide [1]. The term denotes a group of disorders affecting the heart and blood vessels, including coronary heart disease. Coronary heart disease is also known as ischemic heart disease or myocardial ischemia. It can ultimately lead to myocardial infarction [2], commonly referred to as heart attack. It has been proposed that strain and strain rate imaging can serve as non-invasive tools for quantitative assessment of regional myocardial contractility [3, 4] and detection of myocardial ischemia and infarction [5, 6, 7, 8]. Cardiac motion and deformation are closely related and hence, myocardial velocity measurements can be used to obtain global and regional strain and strain rate data [8]. Myocardial motion and strain can be measured non-invasively using for instance MRI [9, 10] or ultrasound [11, 12]. However, ultrasound motion estimation techniques will be the focus of this thesis.

Over the last decades, diagnostic ultrasound has experienced tremendous development and growth [13]. Ultrasound is known as a relatively cheap, non-invasive, non-ionizing, bedside imaging modality, which is fast, easy to use and able to provide real-time images [4, 14]. It is commonly associated with the imaging of fetuses in the utero. However, there is a wide range of medical applications of ultrasound, including measurement of blood flow using Doppler techniques [15], measurements related to the stiffness of tissue [16] and cardiac imaging [17]. Tissue Doppler imaging (TDI) is an ultrasound technique proposed for myocardial motion estimation [18]. The main challenge of this method is that it measures only the axial velocity component, yielding one-dimensional motion estimates. Because of the 3D nature of cardiac motion, a 3D motion estimation scheme must be applied in order to be able to measure the full myocardial motion. Several techniques have been proposed for motion estimation in two and three dimensions, such as speckle tracking [19, 20] and cross-beam techniques [21, 22, 23]. In this study, a novel cross-beam technique will be presented, and the performance of this motion estimator will be compared to two similar cross-beam techniques in addition to speckle tracking.

1.1 State of Research

The starting point of this thesis is the specialization project presented in [24], where a cross-beam technique for 2D myocardial motion estimation, implemented using Python,

is described. This motion estimator is based on the introduction of transverse oscillations (TOs), a technique first proposed by Jensen and Munk in [25] and Anderson in [26]. In this context, TOs denote a received 2D ultrasound field featuring oscillations in both the transverse and the axial direction. The TOs enable motion estimation in the direction transverse to the ultrasound beam. Jensen and Munk described a method that produces TOs by applying a special apodization and focusing scheme. Later, Varray and Liebgott have proposed a new method for two-dimensional motion estimation based on TOs produced by filtering [27]. The filtering-based TO approach was combined with a phase-based motion estimation technique and ultrafast imaging by Salles et al. to develop a high frame rate 2D motion estimator [28]. This motion estimation scheme served as the basis for the work done in [24].

Both Jensen's research group and Salles et al. have proposed TO methods for motion estimation in three dimensions [29, 30, 23]. Jensen's method has been applied to blood flow, while the method proposed by Salles et al. has been used to estimate the motion of tissue. Jensen's 3D method is an extension to the 2D approach, where each velocity component is estimated separately by introducing TOs in one transverse direction at a time. The method developed by Salles et al. is built on the introduction of TOs in both transverse directions simultaneously, and the estimation of motion using a 3D extension to the phase-based motion estimation scheme.

1.2 Goal and Scope

The aim of this study is to compare 3D motion estimation methods based on TOs produced by three different filtering schemes. Two of the filtering schemes are based on previous work and publications [29, 30, 23], while the third is a novel approach. The methods will be validated against 3D speckle tracking when applied to experimental data acquired from a phantom with 1D linear motion or 3D circular motion. To show the potential of clinical application, the methods will be tested on a 3D *in vivo* example from a healthy human heart. Specifically the goals of the thesis are summarized as follows:

1. Compare three different filtering schemes for introducing TOs to estimate 3D tissue motion in terms of accuracy and computational efficiency

2. Compare the three TO methods to 3D speckle tracking

3. Perform experiments using a 2D matrix array transducer to acquire 3D ultrasound data which can be used in validation and comparison of the motion estimation techniques presented

1.3 Outline of Thesis

The thesis is organized as follows. Section 2 covers the main theoretical concepts forming the basis of the thesis. This section consists of several parts. First, the basic principles related to the physiology of the heart are presented, as the study is aimed at cardiac applications. Then, ultrasound with main focus on echocardiography and 3D imaging is reviewed. This part is followed by an introduction to ultrafast ultrasound imaging and plane wave imaging. Tissue motion estimation is then presented, with tissue Doppler imaging for 1D estimation and speckle tracking and cross-beam techniques for 2D and 3D estimation. The cross-beam technique known as TO imaging is described in further detail, followed by an introduction to phase-based motion estimation. Section 3 presents details regarding the implementation of the motion estimation procedures, in addition to describing the experimental trials carried out in order to be able to validate and compare the different methods. Results from the application of the motion estimators to different sets of data are presented in Section 4, while the results are discussed in Section 5. The concluding remarks of the thesis are given in Section 6. Relevant source code and the abstract submitted for the IUS 2017 conference can be found in Appendices A and B, respectively.

2 Theory

An introduction to the theoretical principles that form the basis of the thesis will be given in this chapter. As the motion estimation methods aim at estimating the motion of cardiac tissue, the main functions and physiology of the heart will be presented. The focus of the thesis is on 3D motion estimation techniques, which are based on 3D ultrasound data. Hence, the principles of 3D ultrasound imaging will be given, as well as an introduction to different techniques proposed for motion estimation in 1D, 2D and 3D. These techniques include tissue Doppler imaging, speckle tracking and motion estimation based on TOs.

2.1 Physiology of the Heart

The following section is based on the description of the main functions and physiology of the heart given by VanPutte et al. in [31]. The heart is a muscle, and responsible for pumping blood to the rest of the body through the blood vessels. The blood, the blood vessels and the heart make up the cardiovascular system. The heart wall is built up of three layers of tissue: The epicardium (outer layer), the myocardium (middle layer) and the endocardium (inner layer). The myocardium is the thickest layer and consists of muscular cells. It is responsible for the contraction of the heart. A healthy, adult heart is approximately the size of a closed fist and is located slightly to the left of the mid-line of the sternum in the thoracic cavity between the lungs. It consists of four chambers: the left and right atria, in addition to the left and right ventricles. Figure 2.1 illustrates the heart and its location.

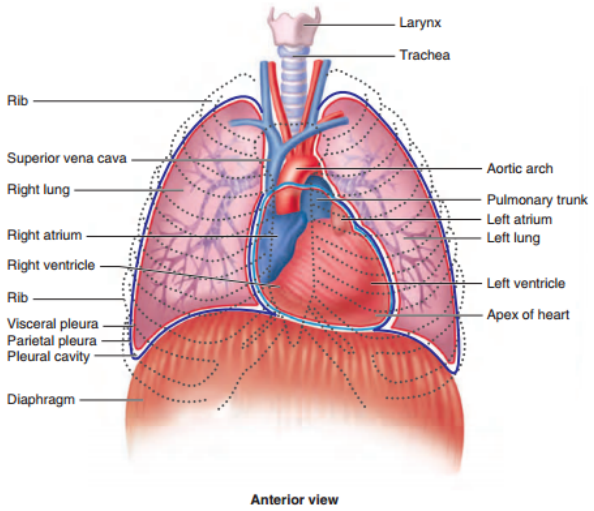

Figure 2.1: The heart and its location. From [31].

The right side of the heart is responsible for pumping blood through the pulmonary circulation, making the blood flow from the right ventricle to the lungs and back to the left atrium. The left side of the heart is responsible for pumping blood through the systemic circulation, making the oxygenated blood flow from the left ventricle to tissues all over the body and back to the right atrium. Figure 2.2 displays the circulatory system with the atria and ventricles. It also shows the blood flow through the pulmonary and systemic circulations.

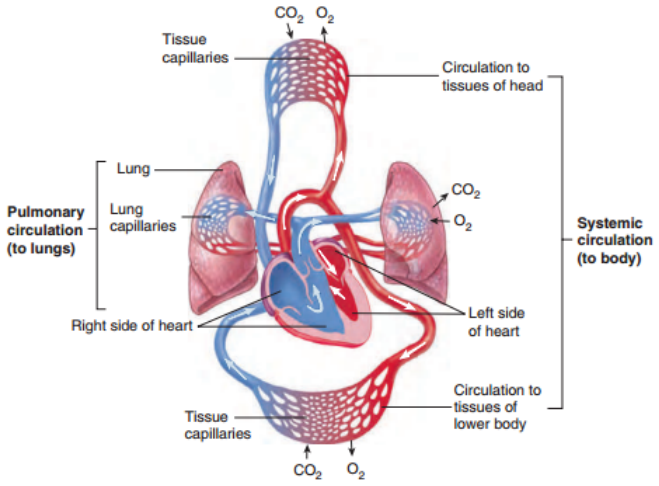

Figure 2.2: The circulatory system. From [31].

The heart cycle can be divided into two main intervals regarding time: Systole and diastole [4]. During systole, the left ventricle contacts in order to force blood to flow into aorta [32]. This contraction is caused by a combination of circumferential twisting and longitudinal shortening of the ventricle. As the apex of the heart is relatively stationary throughout the heart cycle, it is the mitral plane, separating the left atrium and the left ventricle, that moves towards the apex during shortening. The shortening process results in a radial thickening of the walls of the left ventricle. Relaxation of myocardial fibres, elongation and untwisting occurs during diastole and causes a thinning of the walls as the ventricle is refilling with blood.

2.2 Echocardiography

Echocardiography is a term denoting ultrasound applied to the heart. It is one of the most important non-invasive imaging techniques for cardiologists [33], and can for instance be used in the quantification of regional myocardial function. This has traditionally been done by visual inspection of the motion of the tissue, in combination with measurements of the thickening and thinning of the cardiac wall [34]. However, it has been shown that changes in contractility of the heart is closely related to changes in both deformation and segmental systolic velocities [35, 36]. Therefore, regional velocities, strain and strain rate have been proposed as indices of regional myocardial function. These are measures that can be provided by tissue Doppler imaging, an ultrasound technique which will be described later. However, quantifying regional myocardial function by the velocity has several drawbacks. First, the angle between the ultrasound beam and the direction of motion influences the peak velocity measurement. This is referred to as the angle dependency of the Doppler techniques. Second, the overall motion of the heart may influence the estimated regional velocity. This can be referred to as the tethering effect, and implies that the velocity of a given segment might be influenced by contraction in adjacent tissue segments. Tethering effects make it challenging to distinguish between actively contracting and passively moving tissue when the velocity is used as the source of information. Therefore, strain and strain rate, which are based on the velocity gradients, are preferred for quantification of regional myocardial function.

The principles of cardiac strain were first formulated by Mirsky and Parmley [37]. Strain is defined as deformation of tissue due to applied stress [38, 12] and strain rate as the speed at which strain or deformation occurs [12]. As these indices measure relative motion, known as deformation, they can be used to discover stiff and non-contracting tissue in the myocardium. The reader may refer to [12] for more details regarding strain and strain rate imaging.

2.3 3D Ultrasound Imaging

3D ultrasound has shown to be useful in imaging of the heart, and also in myocardial motion estimation as a cause of the 3D nature of the cardiac motion. A brief introduc-

tion to 3D ultrasound imaging will therefore be given in the following. The introduction to 3D ultrasound imaging given by Holm in [39] will serve as the basis for this section. 3D ultrasound imaging was developed during the 1990s. Originally, the 3D image was constructed by combining multiple 2D images by tilting, rotating or moving the probe along a straight line. The first usable 2D matrix array probes were introduced in 2004. Such probes are based on a matrix array of elements and can be steered in two directions. Hence, 2D matrix array probes allow 3D imaging without mechanically moving the probe. Figure 2.3 shows how the 2D matrix array can be steered in two directions, creating the 3D volume. It also shows three orthogonal image planes retrieved from the image volume.

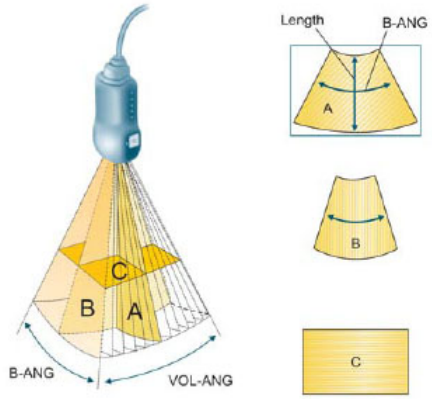

Figure 2.3: 3D image volume resulting from 3D acquisition using a 2D matrix array transducer. From [40].

Today, the use of 3D ultrasound is increasing as it overcomes the problem of conventional 2D ultrasound to view 3D structures in a 2D image [41]. The main challenges of 3D ultrasound imaging are related to the large number of elements in the matrix array. A typical beamformer has 128 channels. To process all the approximately 3000 elements of a fully sampled 2D matrix array would require a large receive path of the beamformer, an excessive amount of power and have an extreme cost [42]. In order to avoid these difficulties, parts of the beamforming is performed in the probe using low power technologies. The rest of the beamforming is performed in the scanner. The large number of elements and hence the large amount of data per image frame compared to conventional 2D ultrasound, constitute a challenge regarding the frame rate because of the limited PRF. Multiline acquisition, a technique where multiple image lines are retrieved from one ultrasound beam, must therefore be applied in order to achieve an acceptable frame rate. 3D ultrasound has several areas of use, such as obstetrics and imaging of organs in the abdomen. However, 3D ultrasound has shown to be useful also in cardiovascular applications [43].

2.4 Ultrafast Ultrasound Imaging

In conventional ultrasound, focused ultrasound beams are used to sequentially insonify the given medium and reconstruct one image line from each transmitted beam [44]. The number of ultrasound beam firings necessary to create one image frame in this manner equals the number of image lines in the frame. This leads to the time required to build an image frame:

$$T_{image} = N_{lines} * \frac{2z}{c} = \frac{N_{lines}}{PRF_{max}} \tag{2.1}$$

where c is the speed of sound in the medium, z is the imaging depth and N_{lines} is the total number of lines in one image frame. The maximum pulse repetition frequency (PRF) is given by $\frac{c}{2z}$, because an ultrasound pulse cannot be fired before the previous pulse has returned to the transducer. The speed of sound is assumed to be constant 1540 m/s in human tissue. With a given T_{image}, the maximum frame rate possible to achieve is given by:

$$FR_{max} = \frac{1}{T_{image}} \tag{2.2}$$

The maximum frame rate possible to achieve using this conventional approach is limited. Echocardiography and 3D imaging are examples of ultrasound applications requiring even higher frame rates. Echocardiography aims at capturing the motion of the heart, and hence higher frame rates are required as the heart is a fast moving structure. Typically, a frame rate of 30-60 frames/s is required in order to display the cardiac motion adequately [45]. Regarding 3D ultrasound imaging, the number of lines in a 3D image is significantly higher than in a 2D image, as it is built up of multiple 2D images. Hence, it is necessary to increase the 2D frame rate in order to obtain a satisfactory 3D frame rate. As an example, imaging a structure at 15 cm depth yields a PRF_{max} of $\frac{1520m/s}{2*15*10^{-2}m} = \approx 5000Hz = 5kHz$. A 3D volume consisting of 100 × 100 image lines will then result in a maximum frame rate of $\frac{5kHz}{100\times100frame^{-1}}$ = 0.5 frames/s, a frame rate far from the requirement of 30-60 frames/s for cardiac imaging. Multiline acquisition has been proposed to increase the frame rate, as this technique allows for multiple image lines to be retrieved per ultrasound beam. Other approaches such as limiting the field-of-view, reducing the line density and volume stitching have also been suggested to increase the frame rate [46]. However, higher frame rates are achieved at the cost of poorer image resolution.

When imaging fast moving structures such as the heart, even higher frame rates than what is possible to achieve with multiline acquisition and the other techniques mentioned might be necessary. This is in order to be able to capture small displacements and limit aliasing effects when estimating the phase shifts between consecutive image frames. To achieve an even higher frame rate, an ultrafast ultrasound imaging scheme can be used. The architecture of such a system is different than the architecture of a conventional ultrasound system [44], as the desired number of image lines can be reconstructed in parallel from one single transmit beam. Hence, the entire image frame

can be built from one single ultrasound beam, yielding a frame rate limited only by the time of flight for one pulse:

$$T_{image} = \frac{2z}{c} \tag{2.3}$$

Myocardial motion estimation [47, 46] and myocardial perfusion imaging [48, 46] are some of the clinical targets proposed for ultrafast ultrasound imaging. Jensen et al. showed that vectorial flow motion can be estimated when an ultrafast imaging system is used to implement synthetic aperture imaging techniques [49, 50]. Synthetic aperture imaging denotes a technique where multiple low-resolution images are combined into a high-resolution image.

2.4.1 Plane Wave Imaging

One of the most common techniques used to achieve ultrafast imaging is the plane wave approach, as described by Montaldo et al. in [51]. In order to construct a plane wave, all transducer elements are excited simultaneously. Hence, focusing cannot be applied on transmit. This restriction reduces the image quality in images constructed by plane wave imaging. According to Montaldo et al., the beamforming process is a matter of applying delays and summations to the RF signals like in conventional dynamic receive focusing. However, unlike conventional ultrasound imaging, the same set of RF data, subjected to different combinations of delays, is used to construct all image lines in an image frame. Another beamforming method, working in the Fourier domain, has also been proposed for beamforming the plane wave RF data [28, 52, 53].

As the poor resolution of the resulting beamformed images is a major challenge of plane wave imaging, the previously mentioned synthetic aperture imaging technique has been proposed to deal with this problem. This approach combines multiple low-resolution images obtained at different insonification angles in order to synthesize the transmit focus and obtain a high-resolution image.

2.5 Tissue Doppler Imaging

As previously stated, the ability to measure the velocity of the myocardium has shown to be of clinical interest. The ultrasound technique known as tissue Doppler imaging (TDI), also referred to as tissue velocity imaging (TVI), can give quantitative information on the velocity of tissue [18]. This method enhances the principles of conventional Doppler ultrasound to measure tissue motion, instead of blood flow. Pulsed wave (PW) Doppler was used to detect myocardial motion as early as in the 1960s and 1970s [54, 55], even though TDI was not used extensively until the late 1980s [56]. With color-coding of the TDI, developed in the 1990s [11, 57, 58], the method was gaining clinical acceptability. TDI is mainly used for cardiac purposes.

The principle of the Doppler effect in the setting of ultrasound imply that an ultrasound echo will experience a shift of frequency if the medium to be imaged is moving in the

direction of the pulse. This frequency shift can be enhanced to calculate the velocity of moving objects in the image. Conventional Doppler techniques and TDI calculate the velocity based on several ultrasound pulse firings in the same direction. Echoes from these pulses are sampled at a given depth, resulting in a collection of samples from several pulse firings representing this particular position in the image. The resulting signal, consisting of the collection of samples, is known as the Doppler signal. It has a frequency that is related to the velocity of the moving object in the sample region by the following Doppler equation:

$$f_d = 2f_0\frac{v}{c}, \tag{2.4}$$

where f_d is the Doppler shift, f_0 is the center frequency of the transmitted pulse, v is the velocity of the moving object in the direction of the ultrasound beam and c is the speed of sound in the medium. Instead of computing the Doppler shift on each transmitted pulse, the Doppler technique estimates the velocity from phase shifts or time delays between subsequent echoes from the same sample volume using for instance an autocorrelation technique [59]. This is done as a consequence of the Doppler shift being quite small compared to the transmitted pulse bandwidth.

Conventional Doppler ultrasound estimates the velocity of blood flow from echoes returned by moving blood cells. Such cells are small and move fast. Hence, the received signals are characterized by low amplitudes and high Doppler shifts. TDI is used to estimate the velocity of moving tissue, preferably the myocardium. As tissue generally moves more slowly and covers a larger area than blood, the signals reflected from tissue have higher amplitudes and smaller Doppler shifts compared to those returning from moving blood cells [60]. Figure 2.4 depicts the general characteristics regarding the frequency and amplitude of signals returning from moving blood cells and moving tissue.

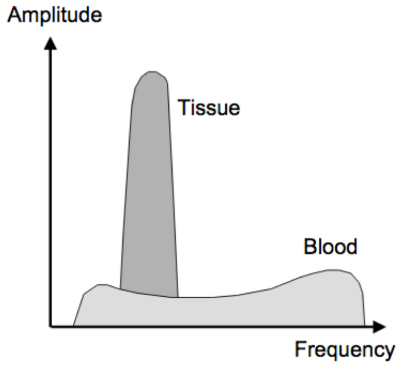

Figure 2.4: Doppler signal model showing that Doppler shifts introduced by tissue typically are lower than those introduced by moving blood cells. In addition, signals returning from tissue generally have higher amplitudes than signals reflected from moving blood cells. From [60].

Despite its extensive use, TDI suffers from several major challenges. The main limitation is related to the angle dependency of the Doppler methods, implying that only the velocity along the direction of the ultrasound beam is measured [61]. Another drawback of the Doppler methods is that due to aliasing effects, they can only estimate velocities lower than half the wavelength of the transmitted ultrasound pulse.

2.6 Tissue Motion Estimation in Multiple Dimensions

TDI can only provide estimates of the axial component of the velocity. To get the full picture of the motion, multiple approaches have been proposed to enable estimation of the second and third velocity component [26, 62, 29, 30, 63]. Such 2D and 3D motion estimation methods are primarily categorized into one of the two categories: speckle tracking and cross-beam techniques.

2.6.1 Speckle Tracking

Speckle tracking was first proposed to estimate the 2D blood flow velocity [62]. In [64], Trahey et al. describe the physical principles of the technique. Speckle tracking is based on the observation that acoustical images of blood and other tissues such as the liver and the myocardium display a textured pattern, also referred to as a speckle pattern. The speckle pattern originates from reflections of the ultrasound waves from many scatterers contained in the tissue [18]. The echo at the transducer surface is a result of the interference between the individual reflections. The positions of the scatterers relative to the transducer determine how the reflections interfere and hence the distribution of gray values in the resulting ultrasound image. The speckle pattern is assumed to be unique for each segment of tissue, and can therefore serve as an acoustical fingerprint. Speckle tracking is thus based on the assumption that when a particular segment of tissue moves, the acoustical fingerprint will move accordingly and make it possible to track the motion.

With the emergence of 3D ultrasound imaging, it has become possible to extend the speckle tracking algorithm to estimate the motion in three dimensions [63]. 3D speckle tracking enables tracking of the real motion in 3D space, not just the 2D motion or a projection of 3D motion into a 2D plane, which is the case with 2D speckle tracking.
Several approaches have been proposed to track the speckle patterns in ultrasound images, among which block matching is an important category [18]. The block matching technique has been proposed for both 2D [64] and 3D [63] speckle tracking. This technique is based on the selection of a 2D or 3D region in the image, referred to as the kernel, and the search for this kernel in the subsequent image frame. Searching for the kernel is done by determining the similarity between the observed pattern at different positions in the subsequent image frame and the kernel. The set of regions that the kernel is matched against in the subsequent frame is usually referred to as the search window or search region. The new position of the speckle pattern is assumed to be at

the position where the similarity has its maximum. Figure 2.5 illustrates the principle of 2D block matching.

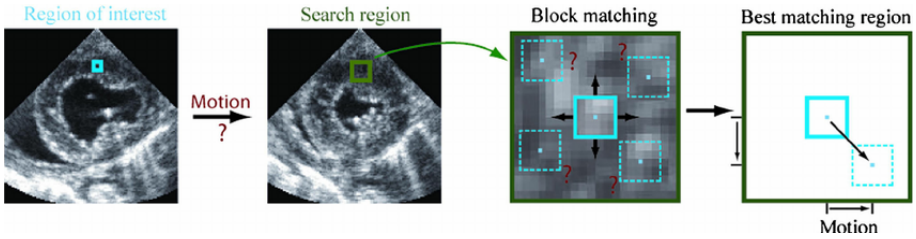

Figure 2.5: The principle of block matching shown for a 2D example. From [65].

In order to obtain a dynamic velocity vector field, the given block matching procedure must be repeated for all image points and between all pairs of subsequent frames in the sequence of ultrasound image frames.

A variety of similarity measures have been defined for 2D block matching [66, 33]. These can be extended for use in 3D applications. A brief introduction to the most common similarity measures for use in block matching will be given in the following, when adapted from 2D to 3D.

Normalized Cross Correlation

The normalized cross correlation (NCC) approach, determines the position of the kernel, here denoted C (current area), in the subsequent image frame by shifting the kernel pixel-by-pixel across the search window, here referred to as R (reference area), and calculating the NCC coefficient at each location. The best match is given by the maximum NCC coefficient. In other words, a coefficient matrix containing the NCC coefficients for all possible locations of the kernel within the search window is computed. According to Hii et al. [67], the NCC coefficients are given by the following equation, when adapted to 3D.

$$NCC_{u,v,w} = \frac{\sum_{x,y,z}(R(x,y,z) - \overline{R_{u,v,w}})(C(x-u,y-v,z-w) - \overline{C})}{\sqrt{\sum_{x,y,z}(R(x,y,z) - \overline{R_{u,v,w}})^2 \sum_{x,y,z}(C(x-u,y-v,z-w) - \overline{C})^2}}, \tag{2.5}$$

where

$$\overline{R_{u,v,w}} = \frac{1}{N_x N_y N_z} \sum_{x=u}^{u+N_x-1} \sum_{y=v}^{v+N_y-1} \sum_{z=w}^{w+N_z-1} R(x,y,z), \tag{2.6}$$

$$\overline{C} = \frac{1}{N_x N_y N_z} \sum_{x=0}^{N_x-1} \sum_{y=0}^{N_y-1} \sum_{z=0}^{N_z-1} C(x,y,z), \tag{2.7}$$

the kernel C is size $N_x \times N_y \times N_z$ and the search window R is size $M_x \times M_y \times M_z$. In addition, the following holds: $N_x \leqslant M_x$, $N_y \leqslant M_y$, $N_z \leqslant M_z$ and $x \in \{0,...,M_x-1\}$, $y \in \{0,...,M_y-1\}$, $z \in \{0,...,M_z-1\}$, $u \in \{0,...,M_x-N_x\}$, $v \in \{0,...,M_y-N_y\}$, $w \in \{0,...,M_z-N_z\}$.

The normalized cross correlation approach is not suitable for tracking the motion of a large number of points in an image, as the computation of the NCC coefficients is computationally expensive [67].

Sum of Absolute Differences

The sum of absolute differences (SAD) approach evaluates the sum of the absolute differences between each pixel in the kernel and the corresponding pixel in the search window, for each position of the kernel in the search window. Adapted to 3D from the 2D version given in [68], the SAD approach is given by

$$SAD = \sum_{i=0}^{N_x-1} \sum_{j=0}^{N_y-1} \sum_{k=0}^{N_z-1} \left| C_{ijk} - R_{ijk} \right|, \tag{2.8}$$

where C (current area) denotes the kernel, R (reference area) is referring to the search window and N_x, N_y and N_z are the sizes of the kernel in x-, y- and z-directions, respectively. The SAD is calculated for all possible locations of the kernel in the search window, yielding a matrix of values. The kernel matches the pattern in the search window best at the position yielding the minimum SAD value.

Sum of Squared Differences

The sum of squared differences (SSD) approach evaluates the sum of the squared differences between each pixel in the kernel and the corresponding pixel in the search window, for each position of the kernel in the search window. The 2D version of the SSD approach is given in [68]. When adapted to 3D, it takes the form

$$SSD = \sum_{i=0}^{N_x-1} \sum_{j=0}^{N_y-1} \sum_{k=0}^{N_z-1} (C_{ijk} - R_{ijk})^2, \tag{2.9}$$

where C (current area) denotes the kernel, R (reference area) is referring to the search window and N_x, N_y and N_z are the sizes of the kernel in x-, y- and z-directions, respectively. Calculating the SSD for all possible locations of the kernel in the search window, yields a matrix of values. The best match between the kernel and the search window is found at the position yielding the minimum SSD value. The SSD approach is slightly more computationally demanding than the SAD approach because of the additional multiplications it introduces.

A novel approach has been proposed for 3D motion estimation, where the axial velocity component is obtained from the conventional autocorrelation method of TDI, while the estimates of the transverse velocity components are given by 2D block matching [69]. This hybrid approach was shown to reduce processing time significantly and improve the 3D motion estimation accuracy compared to regular 3D block matching.

2.6.2 Cross-Beam Techniques

Cross-beam techniques cover a set of approaches proposed for angle-independent motion estimation. Dunmire et al. give an overview of vector-Doppler systems based on such a cross-beam approach in [21]. The development of cross-beam systems for angle-independent velocity measurements started in the 1970s. Early designs proposed to use several single-element transducers to transmit and receive ultrasound beams at different angles. This design was proposed both for 2D and 3D motion measurements. Later, the transmit and receive roles were separated and assigned to different transducers. For the 2D approach, the system consisted of two transmit transducers placed at opposite inclinations with respect to the vertical axis and a receive aperture positioned between the two transmitters at zero angle with respect to the vertical axis. The transmit and receive roles could also be interchanged. By transmitting one beam and receiving at two angles, the frame rate could be increased compared to transmitting two beams and receiving one. Fox described how the 3D velocity vector can be calculated by transmitting multiple beams at different angles into the medium by the use of a six-transducer system [70] or a three-transducer system [22]. The main challenge of the approach involving several transducers, is the need to mechanically adjust the transducers to image varying depths. Therefore, effort was put into developing an approach to overcome this challenge. Papadofrangakis et al. were the first to propose a subaperture approach for 2D estimation of flow components both parallel to and transverse to the ultrasound beam in 1981 [71]. A linear array transducer was divided into three separate parts: one transmit subarray located at the center and two receive subarrays located on either side of the transmit subarray. Hall et al. also described how the 2D velocity vector can be estimated by transmitting one ultraosund beam straight down, and receiving from an angle at each side in [72]. Figure 2.6 illustrates the approach. However, the subaperture technique was first applied by Phillips et al. [73]. With the subaperture approach, a 1D array transducer can be used to measure two of the velocity components by receiving at two different angles, while a 2D matrix array transducer can provide estimates of all three velocity components by receiving at three different angles.

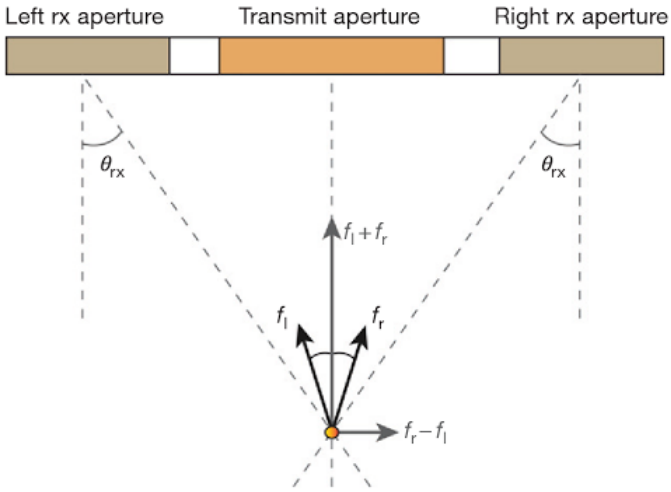

Figure 2.6: The cross-beam technique using one subaperture for transmit and two receive subapertures to calculate the 2D velocity vector. From [74].

2.7 Transverse Oscillation Imaging

Another approach that can be categorized as a cross-beam technique was first proposed by Jensen and Munk in [25] and Anderson in [26]. The method will be referred to as TO imaging in the following. However, it was called the transverse/lateral modulation approach by Jensen and Munk, and the spatial quadrature approach by Anderson. TOs denote a received sound field featuring oscillations in one or both transverse directions, i. e. the directions perpendicular to the beam direction, in addition to the axial direction. The 2D TO approach is based on 2D ultrasound images and aim at generating a sound field oscillating in the transverse direction in addition to the axial direction. The 3D TO approach is based on 3D ultrasound images and aim at generating a sound field oscillating in both transverse directions in addition to the axial direction. The sound field oscillating in one or two transverse directions is created on receive. Hence, it is not the physical acoustic field that is oscillating. The TOs can also be described in 2D as the interference of two ultrasound beams propagating in different directions, creating oscillations in the transverse direction. This is illustrated in Figure 2.7.

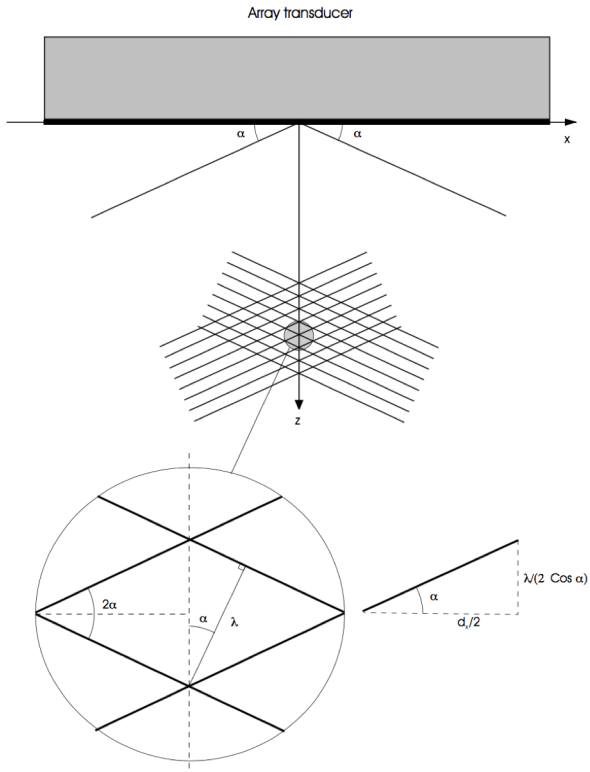

Figure 2.7: Illustration of how the TOs in 2D can be explained as the interference of two ultrasound beams propagating in different directions. From [25].

Several approaches for obtaining TOs have been proposed [25, 27]. The conventional method suggests to apply a special beamforming scheme [25]. Another method has proposed to use a filtering technique to achieve the received sound field featuring TOs [27]. Both of these approaches will be described in the following.

2.7.1 Conventional Transverse Oscillations

According to Jensen and Munk [25], the 2D ultrasound field featuring oscillations in both the axial and the transverse direction can be obtained using a single array transducer in combination with a beamformer specifically developed for the generation of TOs. Jensen and Munk proposed to use an apodization function, typically consisting of two separate peaks, to generate the transversely oscillating field. Generating the lateral modulation mainly on receive offers most flexibility, as it can easily be adapted dynamically to different depths.

According to the Fraunhofer approximation, the lateral sensitivity profile $h(x)$ in the far field can be calculated from the Fourier transform of the receive aperture distribution

$w_r(x)$ [75]. This approximation can be used to show that a receive apodization function consisting of two peaks will generate a received RF image featuring oscillations in the transverse as well as the axial direction, as described by Salles et al. in [28]:

$$w_r(x) = \frac{1}{2}\left(e^{-\pi((x_i-x_0)/\sigma_0)^2} + e^{-\pi((x_i+x_0)/\sigma_0)^2}\right) \tag{2.10}$$

$$h(x) \approx \mathscr{F}\{w_r(x)\} = e^{-\pi(x/\sigma_x)^2} cos\left(\frac{2\pi x}{\lambda_x}\right), \tag{2.11}$$

where x_i is the position of the transducer element, $x_0 = \frac{\lambda z}{\lambda_x}$, $\sigma_0 = \frac{\sqrt{2}\lambda z}{\sigma_x}$, σ_x is approximately the FWHM of the Gaussian envelope, λ_x is the expected transverse wavelength, λ is the wavelength of the transmitted pulse and z is the depth of interest. As can be observed, x_0 and σ_0 are functions of the depth z.

After introducing the lateral modulation, several measurements must be obtained in order to be able to estimate the 2D velocity. The axial component is estimated from conventional phase-shift estimation as in TDI, by acquiring the in-phase and quadrature samples. The transverse component is estimated from a spatial quadrature sampling, where two fields, shifted 90 degrees relative to each other and oscillating in the lateral direction are used. This approach allows for measuring both the magnitude and the sign of the transverse component of the velocity. For a more thorough description, the reader may refer to [25].

The conventional TO method has been used in several applications, including the construction of 2D vector flow maps visualizing the blood flow [76] where it was combined with plane waves, and the construction of 2D displacement maps showing the motion of a simulated left ventricle [77].

The extension of the conventional 2D TO motion estimation approach to 3D is described by Jensen and Pihl in [29, 30]. It suggests that all three components of the velocity vector can be estimated by generating two double-oscillating fields on receive, and applying spatial quadrature sampling using a 2D matrix array transducer. One field is oscillating in the x- and z-directions and the other is oscillating in the y-and z-directions. Hence, this approach assumes that the velocity estimates can be decoupled into three independent velocity components, v_x, v_y and v_z, and estimates each transverse velocity component from a separate sample volume. Salles et al. proposed an extension of the conventional 2D TO method to 3D in [23]. Unlike the 3D approach proposed by Jensen and Pihl, it suggested to produce a field featuring oscillations in all three directions simultaneously in order to estimate the three velocity components.

2.7.2 Transverse Oscillations by Filtering

The main limitation of the conventional TO method is that it is dependent on the beamforming to generate the transversely oscillating field [28], which imply that the raw data must be re-beamformed in order to change the TO parameters. Another drawback of the conventional TO approach is that the TOs are produced using pre-beamformed

data. Such raw data is difficult to access on commercial, clinical scanners [27].

Alternative strategies for producing 2D TOs have been proposed in order to overcome some of the challenges related to the conventional TO method [27]. The alternative approaches described in [27] suggest to produce the TOs by applying convolution or a filtering scheme to the RF or B-mode images. Using RF images, the filtering or convolution needs only be applied to the transverse direction. Oscillations in the axial direction are already present in RF signals, and hence it is necessary to generate oscillations in the transverse direction only in order to achieve a field featuring oscillations in two directions. However, if B-mode images are used, convolution or filtering must be applied to both the axial and the transverse direction. The Fourier transform of the filter described in [28] for this 2D filtering approach, consists of two separate peaks achieved using Gaussian functions. The 2D Fourier transform of the RF image is multiplied with a mask with lines corresponding to the Fourier transform of this 1D filter. The resulting frequency spectrum of an RF image after applying the described 2D filtering-based TO technique consists of four separate ranges of spatial frequency, as shown in Figure 2.8. The widths of the frequency ranges correspond to the bandwidths of the oscillations, while the positions of the frequency ranges give the wavelengths of the oscillations.

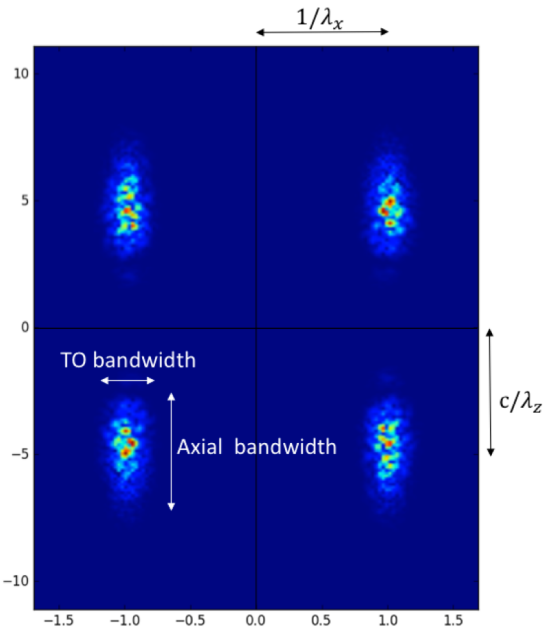

Figure 2.8: K-space representation of a 2D RF image with TOs. This 2D Fourier spectrum contains four separate ranges of spatial frequency. The positions and widths of the frequency ranges correspond to the wavelengths and bandwidths, respectively, in the axial direction and the TOs.

With the filtering technique, the TO parameters such as the bandwidths and the wavelengths of the oscillations can easily be adjusted by changing the size and spacing between the peaks of the filter.

2.8 Phase-Based Motion Estimation

After the construction of RF images containing TOs, the 2D or 3D velocity must be estimated. Salles et al. suggest to use a phase-based motion estimation approach as described in 2D by Basarab et al. in [78]. The extension of this method to 3D is given by Salles et al. in [23]. The phase-based motion estimation is based on creating complex image blocks, also referred to as analytical image blocks, and generating phase images from these. The displacement vectors are calculated from the phase differences between successive, corresponding phase images. The complex image blocks are created using the approach first proposed by Hahn [79], which suggests to keep only one orthant of the Fourier spectrum in order to generate an analytical image. This means that in the 2D case, one quadrant of the 2D Fourier spectrum is kept in order to create a complex image block, while in the 3D case, one octant of the 3D Fourier spectrum is kept. It can be noticed that this is a different way to view the cross-beam technique where one ultrasound beam is transmitted straight down and received at different angles. Keeping one orthant of the frequency spectrum of an image featuring TOs is equivalent to creating a subaperture. With the 2D phase-based motion estimation approach, the motion in the axial and transverse directions (d_z, d_x) between two consecutive image frames can be estimated from the following equations:

$$d_z = \frac{(\Phi_1 - \Phi_2)\lambda_{0z}}{4\pi} \tag{2.12}$$

$$d_x = \frac{(\Phi_1 + \Phi_2)\lambda_{0x}}{4\pi}, \tag{2.13}$$

where Φ_1 is the phase difference between two successive, corresponding analytical images, Φ_2 is the phase difference between a different set of successive, corresponding analytical images, λ_{0z} is the wavelength of the transmitted signal, i.e. the axial wavelength of the RF image, λ_{0x} is the lateral wavelength produced by filtering. Φ_1 and Φ_2 can be calculated from the phase of the autocorrelation functions corresponding to each sequence of analytical images.

Similar equations hold for estimating the three displacement vectors in the 3D extension to the method:

$$d_z = \frac{\Phi_3 + \Phi_1}{4\pi f_z} \tag{2.14}$$

$$d_x = \frac{\Phi_1 + \Phi_2}{4\pi f_x}, \tag{2.15}$$

$$d_y = \frac{\Phi_2 + \Phi_3}{4\pi f_y}, \tag{2.16}$$

where Φ_1, Φ_2 and Φ_3 are the phase differences between successive analytical images corresponding to three independent octants of the Fourier spectrum, and f_z, f_x and f_y are spatial frequencies corresponding to each direction. The full derivation can be found in [23].

The equations are here given in Cartesian coordinates. If a phased array is used in the acquisition, the ultrasound data will be given in polar coordinates for 2D and in spherical coordinates for 3D. In such cases, it is necessary to convert the equations from Cartesian to polar or spherical coordinates. The z-direction will then correspond to the r/axial-direction, the x-direction will correspond to the the θ/azimuth-direction and the y-direction will correspond to the ϕ/elevation-direction.

As mentioned in both [28] and [23], the phase-based motion estimation method is only able to estimate displacements shorter than half the wavelength. However, the method is suitable when applied in combination with ultrafast imaging, as this technique will significantly reduce the magnitude of the inter-frame displacements.

3 Methods

In this chapter, the ideas behind the different aspects of the implementation of the motion estimators are described. Additionally, information on the experimental setups are given.

3.1 Implementation of Motion Estimators Based on Transverse Oscillations

This section covers the implementation of the TO motion estimators. The implementation is based on a 3D extension to the filtering approach described in Section 2.7.2. However, three different filtering schemes were used, including the scheme described in Section 2.7.2. The implementation was done using Matlab, and can be divided into four main parts: Creating subapertures by filtering, calculating the autocorrelation functions, spatial averaging and obtaining the displacement between consecutive images. Each of these parts will be described in the following.

3.1.1 Creating Subapertures by Filtering

The first step in the motion estimation methods based on TOs is to filter the spatial frequency content of the sequence of 3D image volumes. Three different ways of filtering were explored. Each filtering scheme resulted in a received sound field featuring TOs, as a consequence of the corresponding frequency spectra consisting of several separate ranges of spatial frequency. Each separate range of frequency in the filtered frequency spectra can be viewed as a subaperture in the 3D extension to the subaperture approach described in Section 2.6.2. Hence, by extracting the signal received from each subaperture, the Doppler effect can be exploited to calculate different components of the velocity vector depending on the location of each subaperture.

The implementation of the filtering schemes was completed by convolving each transverse image line by a 1D filter. Filtering was performed only in the transverse directions because oscillations are already present in the axial direction of RF images. The convolution was carried out in the frequency domain, treating each transverse direction separately. Filtering in the azimuth direction was performed by multiplying the 1D Fourier transform of the image in the azimuth direction by a mask with lines corresponding to

the Fourier transform of the azimuth filter. Correspondingly, filtering in the elevation direction was performed by multiplying the 1D Fourier transform of the image in the elevation direction by a mask whose lines correspond to the Fourier transform of the elevation filter. Each filter was designed such that its Fourier transform consisted of a Gaussian function. The implementation of the 3D extension to the filtering approach is based on the work done by Salles et al. in [28], where Gaussian functions were used to introduce TOs. Therefore, the filters were designed to consist of a Gaussian function in the Fourier domain. However, other possible choices exists, such as using a Hanning window, Hamming window or a rectangular function.

Figure 3.1 illustrates two 1D filters, each consisting of a Gaussian function. A combination of the two filters can be used to generate two separate ranges of spatial frequency, which will yield TOs in one transverse direction. However, the filters can also be applied separately to extract each of the two subapertures. The Gaussian function can be shifted in order to change the position of the subaperture. In addition, the width of the Gaussian function can be changed in order to adjust the size of the subaperture. It is desirable to keep as much as possible of the original frequency spectrum, in order to keep as much information as possible. This is achieved by using a wide Gaussian function. At the same time it is advantageous to place the subapertures as far apart as possible in order to facilitate estimation of small displacements. The latter is explained by the wavelength of the TOs being dependent on the location of the subapertures, where the wavelength is smaller the closer to the edges of the frequency spectrum. The maximum displacement possible to estimate is limited by half the wavelength of the TOs.

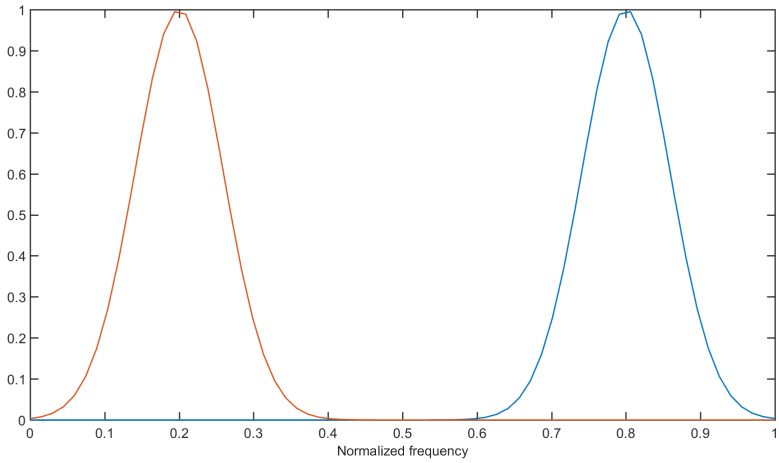

Figure 3.1: Two filters consisting of Gaussian functions. One filter is given by the blue line, and the other is given by the orange line.

As previously stated, three different filtering schemes were developed. Each of these will be described in the following.

Jensen's Approach

The first approach is based on the work done by Jensen's research group. To go from motion estimation in 2D to 3D, it is assumed that the velocity components can be decoupled and estimated independently [29]. Consequently the TOs can be introduced in each transverse direction separately and the transverse velocity components, v_θ and v_ϕ, can be estimated one at a time. This means that the azimuth velocity component is estimated from a field oscillating only in the azimuth and axial directions, and the elevation velocity component is estimated from a field oscillating only in the elevation and axial directions. In total, four subapertures are generated using this approach.

Figure 3.2 shows the spatial filtering scheme in the (f_θ, f_ϕ) plane, where the red ovals illustrate the four subapertures. It can be noticed that the subapertures overlap. Each pair of parallel subapertures can be used to create TOs in the corresponding direction. The subapertures were created by filtering the original spatial frequency content of each image using four different filters. This means that the left subaperture in Figure 3.2 is created by applying a filter consisting of a Gaussian function to the original spatial frequency content of the image, while the right subaperture is created by applying a different filter to the original spatial frequency content of the image. As can be seen from the figure, the filters must be rotated 90 ° in order to generate the upper and lower subapertures compared to the left and right subapertures.

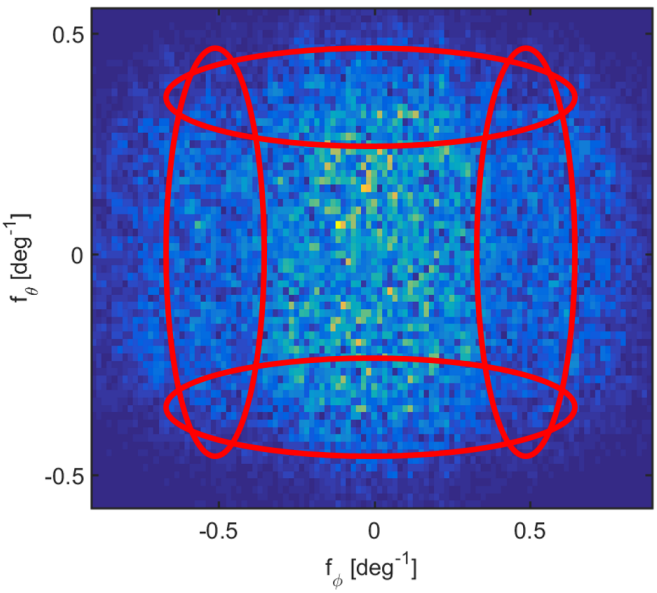

Figure 3.2: The filtering scheme based on the work done by Jensen's research group. The red ovals indicate the locations of the subapertures.

The full implementation of the filtering technique based on Jensen's approach can be

found in Appendix A.1.1.

Four Separate Ranges of Frequency

The second filtering approach is based on introducing oscillations in both transverse directions simultaneously, and is inspired by the work presented by Salles et al. in [23]. The transverse velocity components, v_θ and v_ϕ, are estimated from a field oscillating in both transverse directions simultaneously. Four subapertures were created by applying filters consisting of a Gaussian function to filter the spatial frequency content in both transverse directions. Figure 3.3 illustrates the spatial filtering scheme in the (f_θ, f_ϕ) plane, where the red circles illustrate the four separate subapertures.

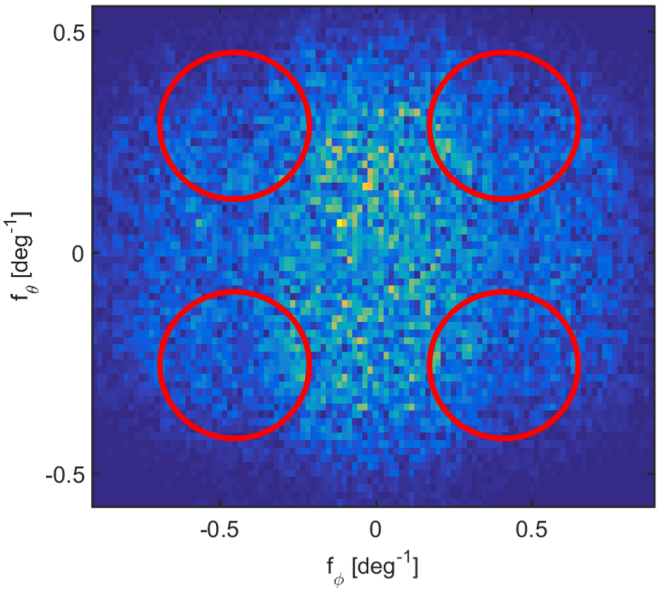

Figure 3.3: The filtering scheme of the method using four separate ranges of spatial frequency to generate TOs. The red circles indicate the locations of the subapertures.

The full implementation of the filtering technique based on keeping four separate ranges of frequency can be found in Appendix A.1.2.

Three Separate Ranges of Frequency

The third approach is based on filtering the spatial frequency content of each image frame to keep only three separate ranges of frequency. Only three subapertures are necessary in order to be able to estimate the three velocity components (v_r, v_θ and v_ϕ). The subapertures are created in a similar manner as described for the first and second approach, by filtering the spatial frequency content using filters consisting of a Gaussian function. Filtering is performed in both transverse directions, and the Gaussian

function is placed carefully in order to generate the desired subapertures. Figure 3.4 shows the spatial filtering scheme in the (f_θ, f_ϕ) plane, where the red circles illustrate the three subapertures created by filtering the original spatial frequency content of each image frame.

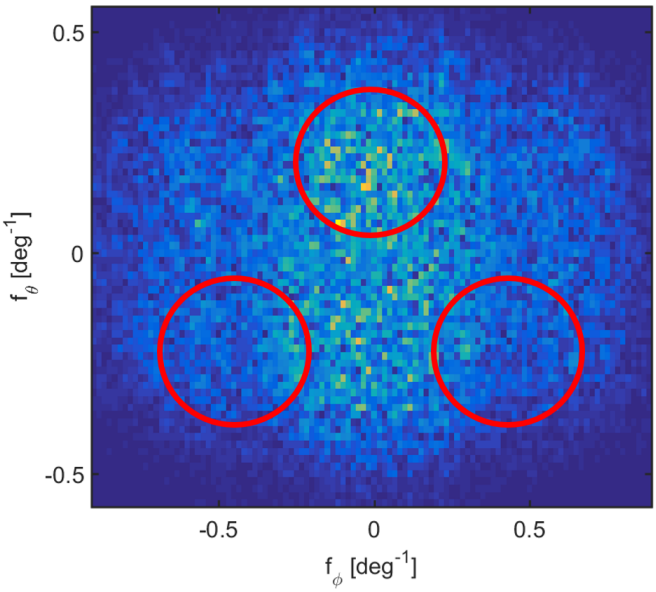

Figure 3.4: The filtering scheme of the method using three separate ranges of spatial frequency to generate TOs. The red circles indicate the locations of the subapertures.

The full implementation of the filtering technique based on keeping three separate ranges of frequency can be found in Appendix A.1.3.

3.1.2 Calculating the Autocorrelation Functions

The autocorrelation technique, where the autocorrelation function is used in ultrasound applications to estimate velocities in blood or other tissues, was first developed for use in applications such as weather radar [80, 81]. The method uses the phase shift between two RF signals to calculate the velocity of the imaged medium at the corresponding point in time. It is the technique implemented on most commercial ultrasound scanners to calculate the axial velocity component [82]. In the motion estimation procedures presented here, the autocorrelation method will be used in the estimation of all three velocity components. To do so, the autocorrelation function corresponding to each subaperture is calculated. The phases of these autocorrelation functions, and hence the velocity estimates, will be at an angle with respect to the z-axis depending on the location of the subaperture. An illustration of the receive angles for the velocity vectors is given in 2D in Figure 2.6. This is the clue for being able to estimate the

transverse velocity components, as the resulting velocity vectors can be combined in different ways in order to yield the transverse velocity components.

3.1.3 Spatial Averaging

Doppler signals are stochastic, meaning that estimates of signal parameters vary randomly. To avoid rapid fluctuations and drop-outs in the final estimates, post-processing techniques such as temporal and spatial averaging are typically applied to the Doppler parameter data [83]. In the implementation presented here, spatial averaging of the autocorrelation functions is applied before calculating the phases. This implies that each autocorrelation value is replaced by an average of itself and the surrounding values. It is likely that adjacent points will behave similarly. Therefore, it can be assumed that spatial averaging will yield acceptable autocorrelation values. In this implementation, spatial averaging of 11 pixels in the axial direction and 5 pixels in each transverse direction was applied. The spatial averaging includes a higher number of pixels in the axial direction than in the transverse directions, because the axial resolution of the images is better than the resolution in the azimuth and elevation directions. The resolution is approximately 1.5 mm in the azimuth direction and 1.8 mm in the elevation direction at a depth of 6 cm, while in the axial direction the resolution is approximately 0.70 mm.

3.1.4 Obtaining the Displacement Between Consecutive Images

Conventional TDI exploits the entire spatial frequency content of the ultrasound images to estimate the axial velocity component. Larger bandwidth, improved spatial resolution and more efficient spatial averaging can be obtained when utilizing the entire spatial frequency content compared to using only parts of it. Therefore, TDI tends to give more accurate estimates of the axial velocity component than a combination of the contributions from multiple subapertures can give. Hence, conventional TDI is the preferred method for estimating the axial velocity component and is therefore used in this implementation. However, the velocity components transverse to the ultrasound beam cannot be estimated based on the entire spatial frequency content of the unfiltered images, as discussed in section 2.5. To estimate the transverse velocity components, i.e. the azimuth and elevation velocity components, the contributions from different subapertures must be combined in two different ways. The transverse velocity components between each consecutive image frame can be calculated from a combination of the phases of the autocorrelation functions related to the different subapertures, while the axial velocity component is calculated from the phase of the autocorrelation function related to the unfiltered images. To calculate the transverse velocity components, the phases must be combined in different ways, depending on the method used. The phase combinations related to the three different methods are given in the following.

Jensen's Approach

Azimuth direction: $\Phi_\theta = \Phi_{Upper} - \Phi_{Lower}$

Elevation direction: $\Phi_\phi = \Phi_{Left} - \Phi_{Right}$

Axial direction: $\Phi_r = \Phi_{All}$

The subscripts are referring to the location of the spatial frequency content of the different subapertures given in Figure 3.2. "All" is referring to the entire spatial frequency content.

Four Separate Ranges of Frequency

Azimuth direction: $\Phi_\theta = \Phi_{UpperRight} - \Phi_{LowerRight}$

Elevation direction: $\Phi_\phi = \Phi_{LowerLeft} - \Phi_{LowerRight}$

Axial direction: $\Phi_r = \Phi_{All}$

The subscripts are referring to the location of the spatial frequency content of the different subapertures given in Figure 3.3. "All" is referring to the entire spatial frequency content.

Three Separate Ranges of Frequency

Azimuth direction: $\Phi_\theta = \frac{\Phi_{LowerLeft}+\Phi_{LowerRight}}{2} - \Phi_{UpperMiddle}$

Elevation direction: $\Phi_\phi = \Phi_{LowerLeft} - \Phi_{LowerRight}$

Axial direction: $\Phi_r = \Phi_{All}$

The subscripts are referring to the location of the spatial frequency content of the different subapertures given in Figure 3.4. "All" is referring to the entire spatial frequency content.

After combining the phases, the velocities are calculated according to (2.14), (2.15) and (2.16). The displacements between each consecutive image frame are given by the corresponding velocity.

The TOs are dependent on several parameters in the implementation. In addition, the estimated trajectory of a point is dependent on the size of the region of interest (ROI)

selected to calculate it. The parameters for the implementation of the TO methods are given in table 3.1.

Table 3.1: TO parameters

Parameter	**Value**
ROI size (Axial, Azimuth, Elevation) [pixels]	(32, 32, 16)
Normalized f_{0x}	0.8, 0.2
Normalized f_{0y}	0.8, 0.2, 0.5
σ_x [mm]	3.5
σ_y [mm]	3.5

Here, f_{0x} and f_{0y} are given as normalized frequencies. They determine the location of the Gaussian function and hence the location of the corresponding subaperture in each direction. The different values given in the table indicate the different normalized frequencies where the Gaussian function is placed in order to create upper, lower, left, right and middle subapertures. σ_x and σ_y determine the width of the Gaussian function and hence the size of the corresponding subaperture in each direction.

3.2 Implementation of Speckle Tracking

3D speckle tracking was implemented using block matching and the SAD approach, as described in Section 2.6.1. The SAD approach was chosen as it is the least computationally demanding of the methods described in Section 2.6.1. Interpolation and a 1D Gaussian approximation scheme, as presented in [84], were applied in order to be able to detect and track sub-pixel motion. Either RF or B-mode images can be used for speckle tracking [85]. However, B-mode images were used in this implementation.

The block matching algorithm is dependent on several parameters. Table 3.2 gives the block matching parameters used in the implementation. These can be adjusted to optimize the performance of the method. The interpolation factor is applied to all three directions. In order to obtain a fair comparison of the TO methods to speckle tracking, the same point and the same ROI were selected for motion estimation using all four approaches.

Table 3.2: Block matching parameters

Parameter	**Value**
ROI size (Axial, Azimuth, Elevation) [pixels]	(32, 32, 16)
Window size (Axial, Azimuth, Elevation) [pixels]	(34, 34, 18)
Interpolation factor	5

3.3 Conversion From Spherical to Cartesian Coordinates

As the motion estimation procedures are aimed at estimating the 3D cardiac motion, the relevant data will be acquired using a 2D matrix array probe. Consequently, the acquired data is given in spherical coordinates. Thus, the motion is estimated in spherical coordinates and needs to be converted to Cartesian coordinates in order be comparable to the true motion. The equations for conversion are given as:

$$v_z = v_r d_r \times cos(\phi) - v_\theta d_\theta r \times sin(\phi) \tag{3.1}$$

$$v_x = v_r d_r \times cos(\theta) sin(\phi) - v_\phi d_\phi r \times sin(\theta) sin(\phi) + v_\theta d_\theta r \times cos(\theta) cos(\phi) \tag{3.2}$$

$$v_y = v_r d_r \times cos(\theta) sin(\phi) - v_\theta d_\theta r \times sin(\theta) sin(\phi) + v_\phi d_\phi r \times cos(\theta) cos(\phi) \tag{3.3}$$

where v_r, v_θ and v_ϕ are the velocities in axial, azimuth and elevation directions respectively, d_r, d_θ and d_ϕ are scaling factors from pixels to mm corresponding to each direction, r is denoting the radial direction, θ is denoting the azimuth direction and ϕ is denoting the elevation direction. Figure 3.5 shows how the azimuth and elevation directions are defined in the 3D image volume. The axial direction is defined to be along the ultrasound beam axis.

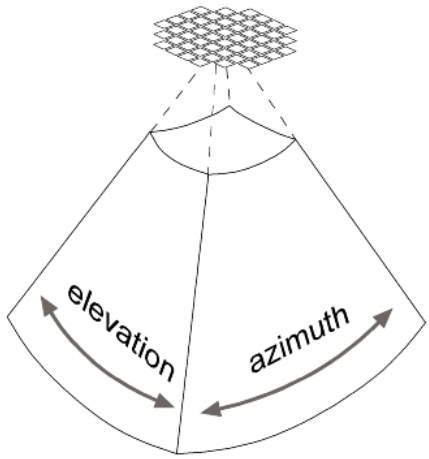

Figure 3.5: The azimuth and elevation directions as defined in the 3D image volume. The axial direction is defined to be along the ultrasound beam axis. From [86].

3.4 Calibration of Spatial Frequency

The motion estimation procedures based on TOs are dependent on the spatial frequencies f_r, f_θ and f_ϕ. In order to produce precise motion estimates, the spatial frequencies must be calibrated according to the relevant sequence of ultrasound data. The spatial frequencies can be calculated theoretically from the frequency spectrum. However, in this implementation, a special calibration procedure was developed. The spatial frequencies were estimated by introducing a known motion, in this case 1 pixel in each direction, to each frame of ultrasound data. Then, the relevant motion estimator was used to estimate the known velocity. From the estimated and known velocities, the spatial frequencies were derived using equations (2.14), (2.15) and (2.16). The calibration of the spatial frequencies was done prior to the motion estimation, and the temporal average of the spatial frequencies estimated for each frame was used in the motion estimators.

3.5 Experimental Trials

In order to be able to verify and compare the motion estimation methods, they were applied to various sets of ultrasound data. Phantom experiments were performed to obtain sequences of ultrasound images featuring uniform, known motion. In addition, the motion estimators were applied to an *in vivo* example with unknown motion. The phantom experiments were performed by moving the probe in a known manner. This enabled the possibility to compare the estimated motion to the ground truth and hence verify the motion estimation methods. In order to be able to compare the estimators in a more realistic setting, an *in vivo* acquisition of a healthy, human heart was obtained. All acquisitions were performed using a locally modified GE Vivid E95 scanner that enabled saving of IQ data.

3.5.1 3D Acquisition of Stepwise Linear Movement in Phantom

An experiment was performed where a phantom was imaged using a 2D matrix array transducer. The probe was moved stepwise between each image frame using a stepper motor. The phantom was filled with water on top, in order to facilitate movement of the probe in the direction perpendicular to the phantom surface. Three different experiments were performed, which in a Cartesian coordinate system can be expressed as:

1. Moving the probe linearly in the x-direction only
2. Moving the probe linearly in the y-direction only
3. Moving the probe linearly in the z-direction only

The introduced inter-frame displacements were 0.1 mm in all directions. A sequence of 20 displacements were introduced in each direction, resulting in a sequence of 21 ultrasound image frames. Moving the probe to introduce the motion resulted in a uniform motion where all points in the image move in the same manner. Table 3.3 gives a list of

the acquisition parameters used. Figure 3.6 shows the experiment setup.

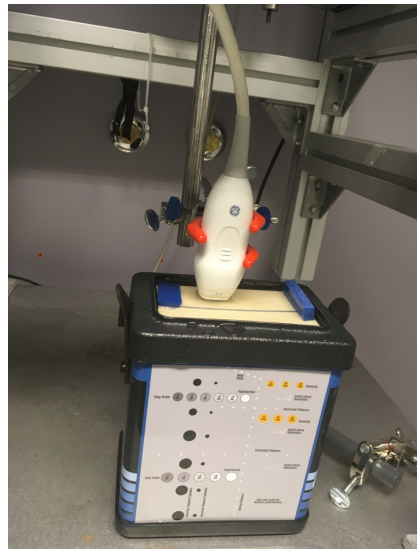

Figure 3.6: Experiment setup showing the probe, how the probe is attached to the stepper motor and the phantom. The phantom is filled with water on top.

Table 3.3: Phantom acquisition parameters

Parameter	**Value**
2D matrix array	4V-D
Pitch	230 μm
Element focus	77 mm
Aperture	24 mm × 21 mm
Number of elements	60x48
Center frequency	2.5 MHz
Demodulation frequency	1.6 kHz
Imaging parameters	
Ultrasound system	Locally modified, university-owned GE Vivid E95
Plane wave compounding	No compounding
Number of plane waves	5x4 plane waves
Imaging depth	12 cm
Volume width	60 ° × 60 °

3.5.2 3D Acquisition of Stepwise Circular Movement in Phantom

Using the same setup as in the case of the linear motion experiments, an experiment where the probe was moved in a circular manner was performed. This experiment was performed in order to be able to test the motion estimators on an induced motion mimicking the real motion of the heart. It enabled the possibility to validate the estimators on three-dimensional motion, i. e. motion in all three directions simultaneously. Figure 3.7 displays the displacement introduced in each of the three directions. Together, the movements form a circle in 3D space. The imaging parameters are given in Table 3.3.

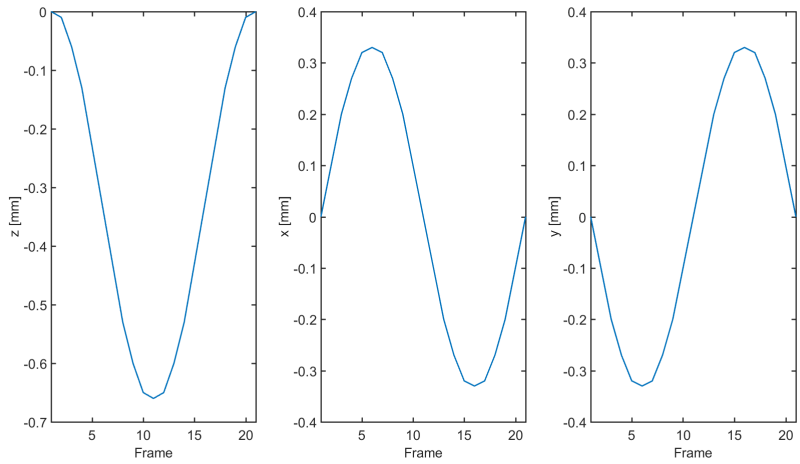

Figure 3.7: The displacement introduced in each of the three directions.

A sequence of 20 displacements were introduced, resulting in a sequence of 21 ultrasound image frames. Moving the probe to introduce the displacements resulted in a uniform motion where all points in the image move in the same manner.

3.5.3 *In Vivo* Acquisition of a Healthy Human Heart Using High Frame Rate

The two previous experiments were performed using using a stepwise motion where each frame of ultrasound data was stored after introducing one displacement step. As the motion estimation methods based on calculating the phases of the autocorrelation functions are restricted with respect to the maximum displacement possible to detect because of aliasing effects, high frame rate imaging is required in order to obtain accurate estimates in real applications. Therefore, it was desirable to test the motion estimators on an *in vivo* example where the data was acquired using high frame rate, in order to test the performance of the estimators in a realistic setting. The imaging parameters for the *in vivo* acquisition of a healthy, human heart using high frame rate imaging are given in Table 3.4.

Table 3.4: *In vivo* acquisition parameters

Parameter	**Value**
2D matrix array	4V-D
Pitch	230 μm
Element focus	77 mm
Aperture	24 mm × 21 mm
Number of elements	60x48
Center frequency	2.5 MHz
Demodulation frequency	1.6 kHz
Imaging parameters	
Ultrasound system	Locally modified, university-owned GE Vivid E95
Plane wave compounding	No compounding
Number of plane waves	5x4 plane waves
Imaging depth	12 cm
Volume width	60 ° × 60 °
Frames per second	820

4 Results

In this chapter, the results from motion estimation using the three TO approaches and speckle tracking will be presented. The motion estimation methods are applied to three different types of ultrasound data: data from a phantom experiment with 1D linear motion, data from a phantom experiment with 3D circular motion and *in vivo* data acquired from a healthy human heart.

4.1 Introduction of Transverse Oscillations

The first step in the motion estimation procedures based on TOs, is to filter the spatial frequency content of every 3D image frame in the sequence of ultrasound data. Filtering is done to divide the receive aperture into several subapertures. The first image frame in the sequence of ultrasound images resulting from the acquisition of the 3D circular movement is used to show the effect of applying the three different filtering schemes. Since the data is three dimensional, only the middle slice of the frequency spectrum in the axial direction is shown. The middle slice of the frequency spectrum corresponds to the axial frequency of 0 Hz in the IQ-data, which equals the demodulation frequency of the RF data. The spatial frequency content is displayed in the (f_θ, f_ϕ) plane. Figure 4.1 shows the unfiltered spatial frequency content of this first image frame.

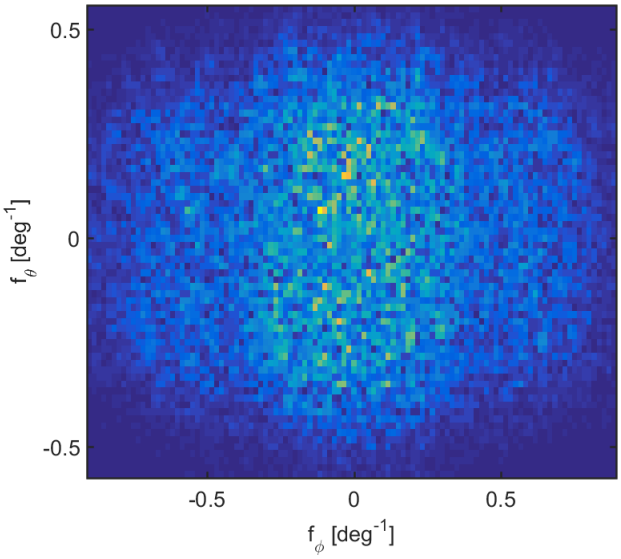

Figure 4.1: The unfiltered spatial frequency content of the first frame of ultrasound data from the acquisition of the 3D circular movement. The dark blue areas indicate zero content of the given spatial frequency. The brighter the color, the higher the content of the given spatial frequency.

Three different schemes have been presented for filtering the spatial frequency content to introduce TOs. Each of these approaches yields a different frequency spectrum after applying the relevant filters to the spatial frequency content of the original image frame. The first approach is based on the work done by Jensen's research group. It was implemented using filtering instead of the special beamforming scheme that was used originally. With this approach, two double-oscillating fields, i. e. fields oscillating in the axial direction in addition to one transverse direction, were created by filtering the spatial frequency content in one of the transverse directions at a time. The resulting (f_θ, f_ϕ) planes of the two frequency spectra are shown in Figure 4.2.

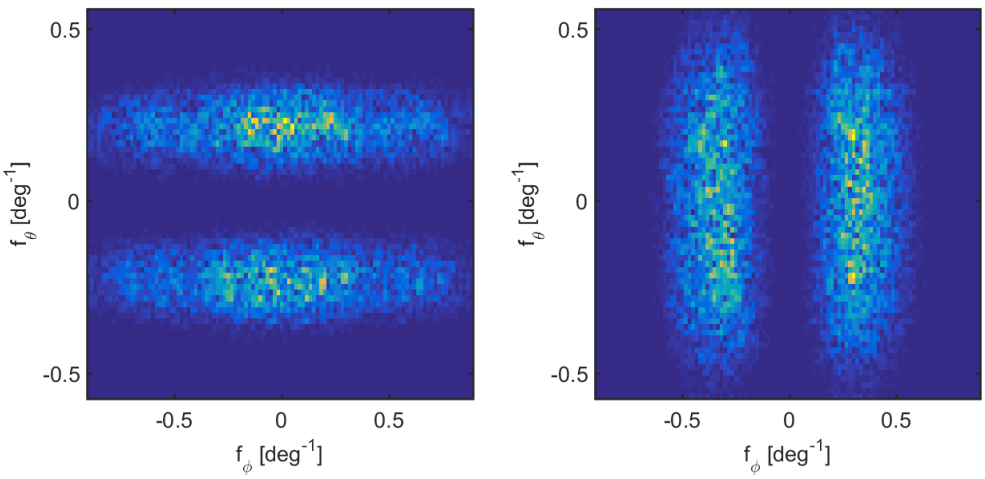

Figure 4.2: The spatial frequency content of the first frame of ultrasound data after applying the filtering scheme as proposed by Jensen's research group. The dark blue areas indicate zero content of the given spatial frequency. The brighter the color, the higher the content of the given spatial frequency.

The figure shows how each frequency spectrum consists of two separate ranges of spatial frequency, resulting in a field featuring oscillations in one transverse direction in addition to the axial. The location of the frequency ranges determines the wavelength of the TOs in each direction.

The second approach is a 3D extension to the method developed by Salles et al. for introduction of TOs by filtering in 2D. The approach has previously been extended to 3D using a similar beamforming scheme as Jensen's research group, while in this thesis it was implemented by applying a filtering scheme. The spatial frequency content of the image frame was filtered in both transverse directions simultaneously to produce a 3D field oscillating in all three dimensions. The resulting frequency spectrum is shown in Figure 4.3.

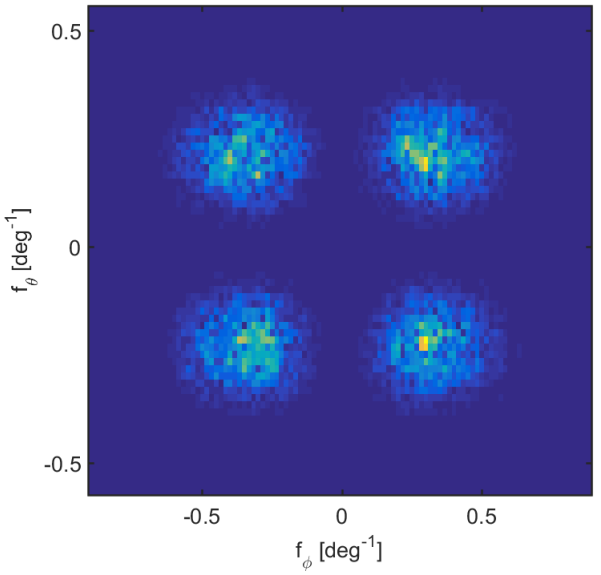

Figure 4.3: The spatial frequency content of the first frame of ultrasound data after applying the filtering scheme yielding four separate ranges of spatial frequency. The dark blue areas indicate zero content of the given spatial frequency. The brighter the color, the higher the content of the given spatial frequency.

It can be observed that the frequency spectrum shows as four separate ranges of spatial frequency. This results in a field oscillating in both transverse directions simultaneously. The wavelength of the TOs in each direction is determined by the location of the four separate ranges of spatial frequency.

A new filtering scheme has been described and proposed for introducing TOs. This approach suggests to produce a field featuring oscillations in three transverse directions simultaneously by keeping only three separate ranges of spatial frequency in the frequency spectrum. Figure 4.4 shows the resulting (f_θ, f_ϕ) plane of the frequency spectrum after applying the relevant filters.

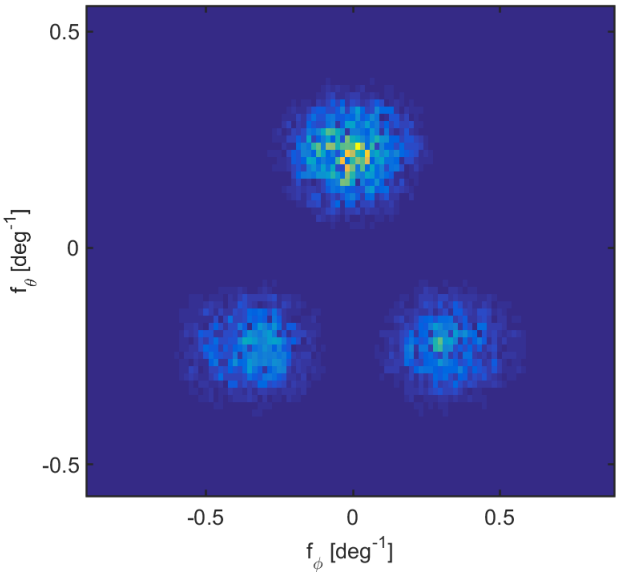

Figure 4.4: The spatial frequency content of the first frame of ultrasound data after applying the filtering scheme yielding three separate ranges of spatial frequency.

In order to extract the three separate ranges of spatial frequency, five different filters were applied to the original spatial frequency content of the image: three to extract the two lower ranges of frequency, and two to extract the upper frequency range.

4.2 Linear Motion

As a first step in the validation and comparison of the four motion estimators, they were applied to a set of one-dimensional, linear motions. The linear motions were introduced mainly in the x-, y- or z-direction separately, and hence these phantom experiments were well-suited to validate the estimates of each component of the motion. Such one-dimensional motion in either x-, y- or z-direction enabled the estimation of each velocity component without being influenced by motion in other directions. In order to be able to compare the three TO methods to the block matching method, the same point was selected for tracking using all four methods. In addition, the same size of the ROI was chosen in all cases. Figure 4.5 displays the point selected to track in the (z, x) plane. The same bright spot in the image was selected to track for all three linear motion experiments.

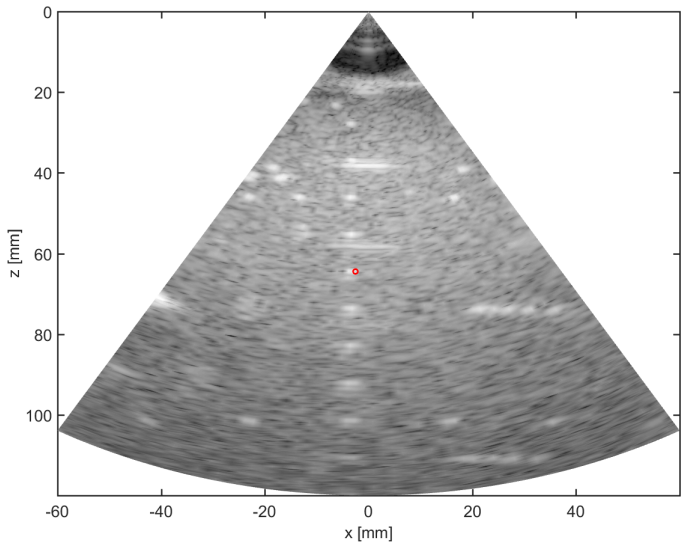

Figure 4.5: The point selected to track for the phantom experiments with linear motion, shown in the (z, x) plane.

4.2.1 Estimated Displacements

The ultrasound images are given in spherical coordinates as a result of the acquisitions being performed using a 2D matrix array transducer. Therefore, the displacements between each consecutive image frame are first estimated in spherical coordinates as pixels. Then, the motion given in spherical coordinates is converted to Cartesian coordinates and expressed in mm. This conversion to Cartesian coordinates is necessary in order to be able to compare the estimated motion to the real motion, which was introduced in Cartesian coordinates. In the case of the linear motions, the ground truth

regarding the motion in each direction is known. Therefore, it is possible to quantitatively compare the estimated motions to the real motion.

Figure 4.6 shows the estimated displacements given in Cartesian coordinates when the real motion is mainly in the z-direction. The black lines indicate the ground truth regarding the displacements introduced in each direction.

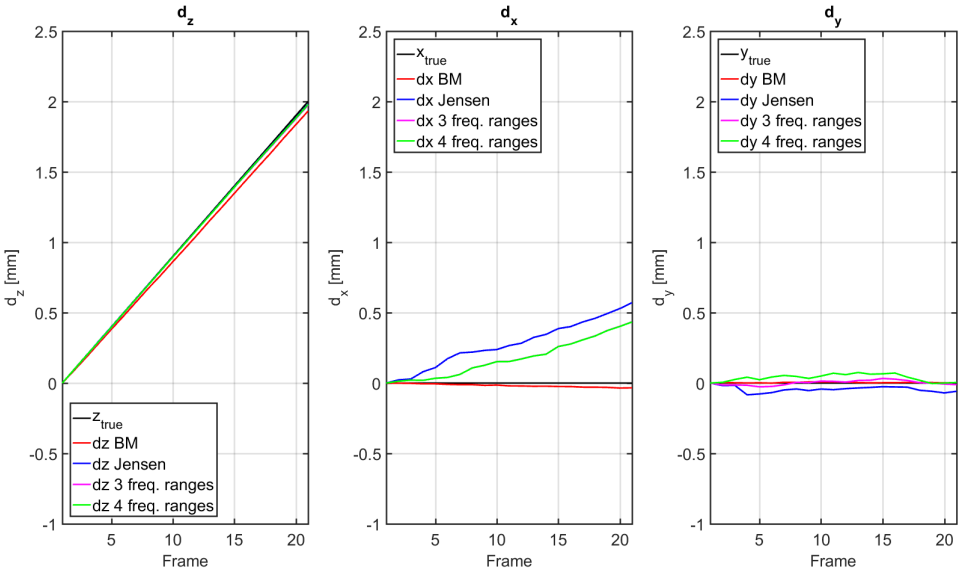

Figure 4.6: Estimated displacements when the real movement is mainly in the z-direction.

Figure 4.7 shows the estimated displacements given in Cartesian coordinates when the real motion is primarily in the x-direction. As before, the black lines indicate the ground truth regarding the motion in each direction.

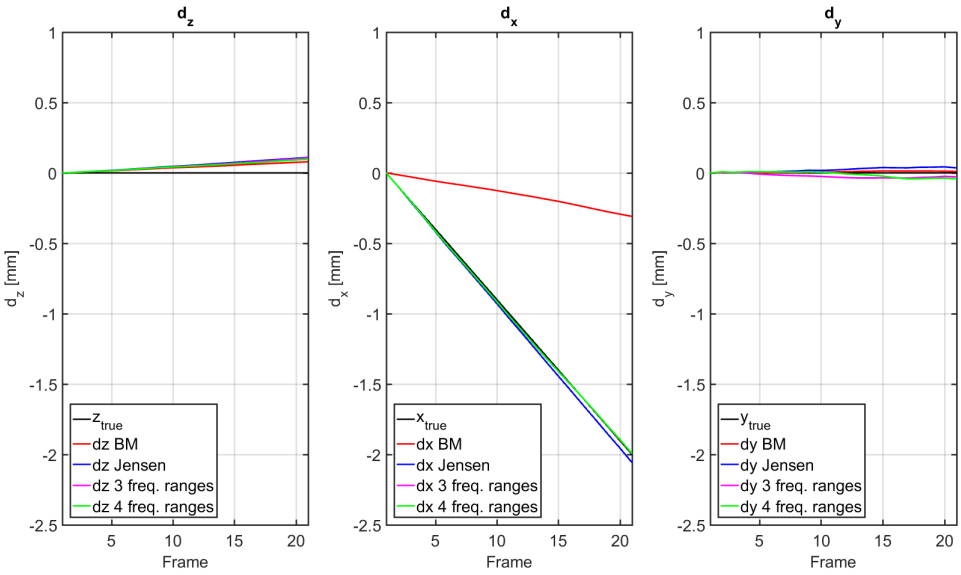

Figure 4.7: Estimated displacements when the real movement is mainly in the x-direction.

In Figure 4.8, the estimated displacements when the real motion is mainly in the y-direction are given in Cartesian coordinates. The black lines illustrate the real displacements introduced in each direction.

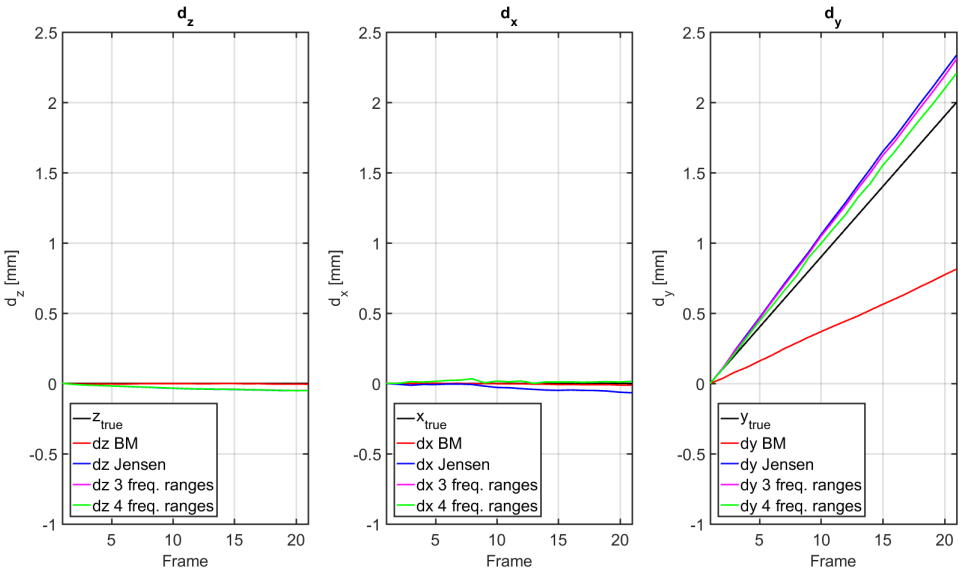

Figure 4.8: Estimated displacements when the real movement is mainly in the y-direction.

It can be noted that the estimates of the z-component from the TO methods seem to be identical. Another important note is that the block matching method seems to underestimate the motion in both transverse directions.

4.2.2 Estimated Velocities

The estimated velocities, given in Cartesian coordinates, are presented in the following, and compared to the true, constant velocity. Three sets of estimated velocities are presented: one where the real motion is mainly in the z-direction, one where the real motion is mainly in the x-direction and one where the real motion is mainly in the y-direction.

Figure 4.9 shows the estimated velocities given in Cartesian coordinates when the real motion is primarily in the z-direction.

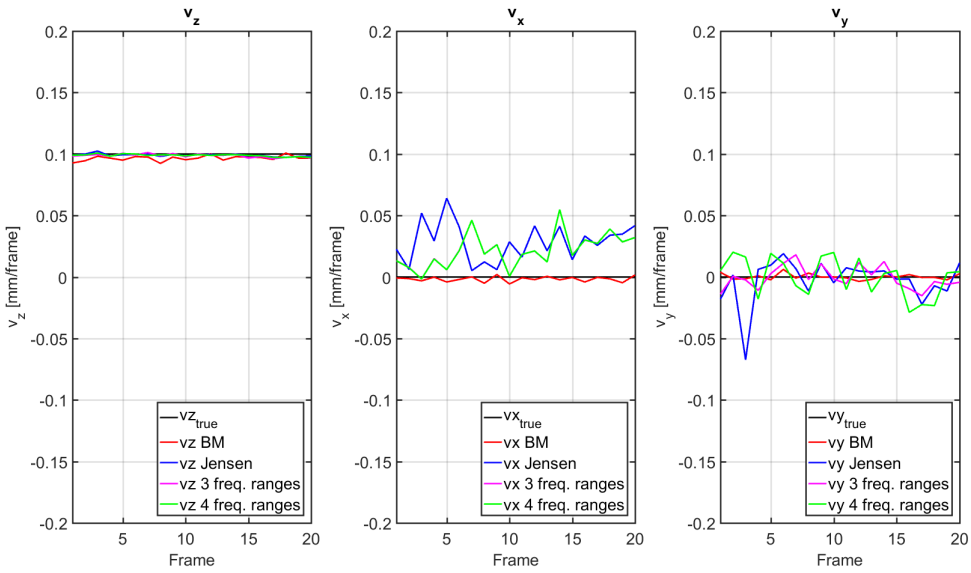

Figure 4.9: Estimated velocities when the real movement is mainly in the z-direction.

It can be observed that the estimated transverse velocities, especially those resulting from the approach proposed by Jensen's research group, show large variations. Despite the true velocities being constant, the estimated transverse velocities are showing a distinct zigzag pattern. Another observation is that the TO methods seem to slightly overestimate the velocity in the x-direction.

Figure 4.10 shows the estimated velocities given in Cartesian coordinates when the real motion is primarily in the x-direction.

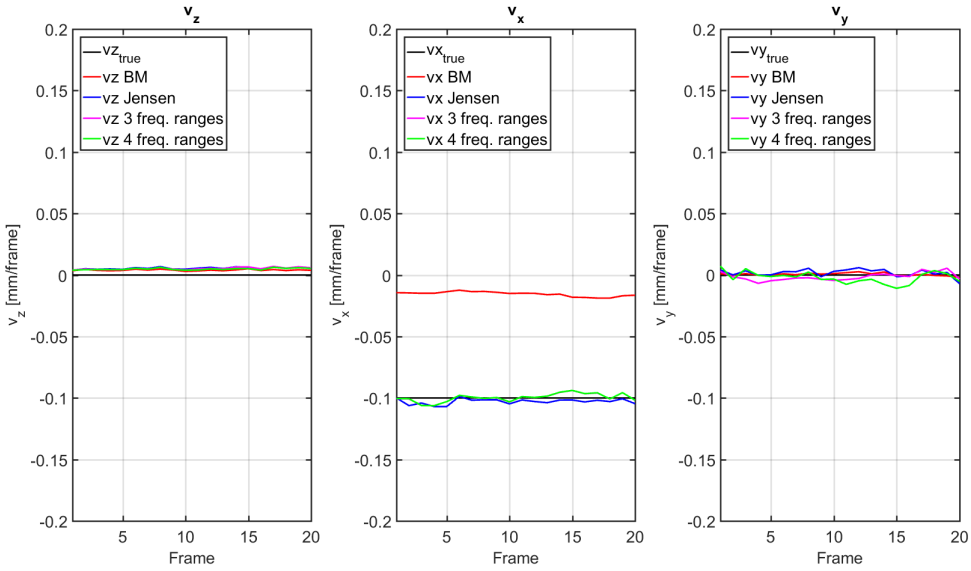

Figure 4.10: Estimated velocities when the real movement is mainly in the x-direction.

The block matching method is clearly underestimating the x-component of the velocity, while the TO methods seem to be yielding similar estimates of this particular velocity component.

Figure 4.11 shows the estimated velocities given in Cartesian coordinates when the real motion is mainly in the y-direction.

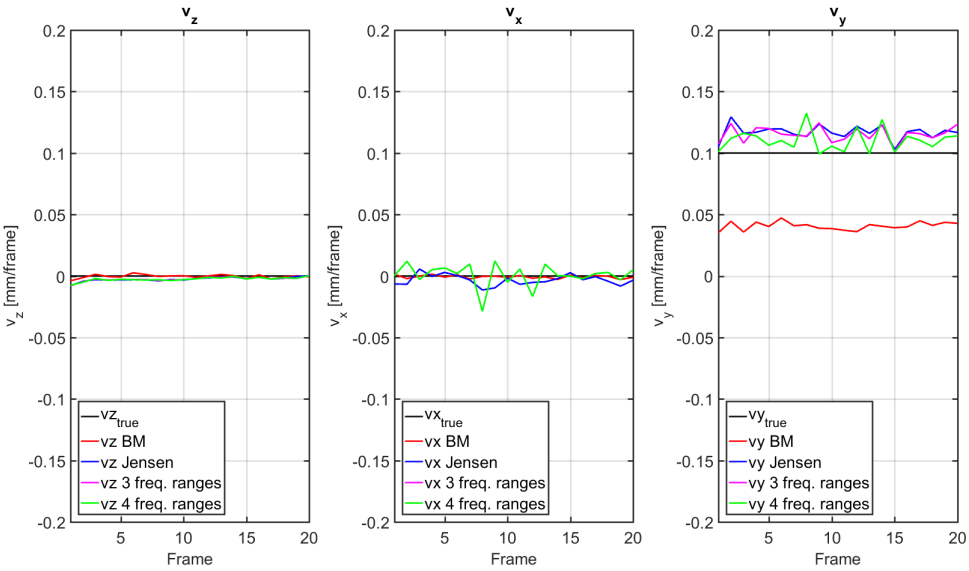

Figure 4.11: Estimated velocities when the real movement is mainly in the y-direction.

Once again it can be noticed that the block matching method seems to underestimate the transverse velocity component, this time in the y-direction. The TO methods seem to slightly overestimate the y-component of the velocity, while all four methods are providing estimates close to the true velocity in z- and x-directions.

4.2.3 Error Measurements

In order to be able to give a quantitative comparison of the four motion estimators, the mean errors and standard deviations are presented for all velocity components in each set of 1D linear motion. Because the errors related to the estimated displacements are accumulating, the error measurements are calculated from the estimated velocities and not from the displacements.

As the velocity is constant in each direction, the mean error of the estimated velocity gives the bias of the estimator, while the square of the standard deviation gives the variance. The bias and variance of an estimator are common measures to characterize its performance. Tables 4.1, 4.3 and 4.5 state the mean errors and standard deviations of each method in each velocity component when the true motion is mainly in the z-, x- and y-direction, respectively. Tables 4.2, 4.4 and 4.6 give the corresponding relative mean errors and standard deviations. The smallest mean error and the corresponding standard deviation in each direction is highlighted in bold.

Table 4.1: Mean errors and standard deviations for the x-, y- and z-component of the velocity for the four different methods when the motion is mainly in the z-direction

True motion in the z-direction	**z-direction**	**x-direction**	**y-direction**
BM [mm/frame]	0.0035 ± 0.0019	**0.0021 ± 0.0018**	**0.0018 ± 0.0016**
TO Jensen [mm/frame]	0.0012 ± 0.00083	0.0285 ± 0.0159	0.0116 ± 0.0143
TO 3 freq. ranges [mm/frame]	0.0016 ± 0.0011	0.0219 ± 0.0142	0.0075 ± 0.0053
TO 4 freq. ranges [mm/frame]	**0.0012 ± 0.00082**	0.0219 ± 0.0142	0.0138 ± 0.0075

Table 4.2: Relative mean errors and standard deviations for the x-, y- and z-component of the velocity for the four different methods when the motion is mainly in the z-direction

True motion in the z-direction	**z-direction**	**x-direction**	**y-direction**
BM	3.5 % ± 1.9 %	**2.1 % ± 1.8 %**	**1.8 % ± 1.6 %**
TO Jensen	1.2 % ± 0.83 %	28.5 % ± 15.9 %	11.6 % ± 14.3 %
TO 3 freq. ranges	1.6 % ± 1.1 %	21.9 % ± 14.2 %	7.5 % ± 5.3 %
TO 4 freq. ranges	**1.2 % ± 0.82 %**	21.9 % ± 14.2 %	13.8 % ± 7.5 %

Table 4.3: Mean errors and standard deviations for the x-, y- and z-component of the velocity for the four different methods when the motion is mainly in the x-direction

True motion in the x-direction	**z-direction**	**x-direction**	**y-direction**
BM [mm/frame]	**0.0039 ± 0.00056**	0.0845 ± 0.0019	**0.00099 ± 0.00076**
TO Jensen [mm/frame]	0.0055 ± 0.00080	0.0030 ± 0.0021	0.0028 ± 0.0020
TO 3 freq. ranges [mm/frame]	0.0053 ± 0.00090	**0.0026 ± 0.0021**	0.0030 ± 0.0017
TO 4 freq. ranges [mm/frame]	0.0049 ± 0.00075	**0.0026 ± 0.0021**	0.0041 ± 0.0030

Table 4.4: Relative mean errors and standard deviations for the x-, y- and z-component of the velocity for the four different methods when the motion is mainly in the x-direction

True motion in the x-direction	**z-direction**	**x-direction**	**y-direction**
BM	**3.9 % ± 0.56 %**	84.5 % ± 1.9 %	**0.99 % ± 0.76 %**
TO Jensen	5.5 % ± 0.80 %	3.0 % ± 2.1 %	2.8 % ± 2.0 %
TO 3 freq. ranges	5.3 % ± 0.90 %	**2.6 % ± 2.1 %**	3.0 % ± 1.7 %
TO 4 freq. ranges	4.9 % ± 0.75 %	**2.6 % ± 2.1 %**	4.1 % ± 3.0 %

Table 4.5: Mean errors and standard deviations for the x-, y- and z-component of the velocity for the four different methods when the motion is mainly in the y-direction

True motion in the y-direction	**z-direction**	**x-direction**	**y-direction**
BM [mm/frame]	**0.0011 ± 0.0010**	**0.0012 ± 0.00089**	0.0593 ± 0.0032
TO Jensen [mm/frame]	0.0026 ± 0.0017	0.0045 ± 0.0031	0.0168 ± 0.0059
TO 3 freq. ranges [mm/frame]	0.0026 ± 0.0017	0.0066 ± 0.0069	0.0154 ± 0.0063
TO 4 freq. ranges [mm/frame]	0.0026 ± 0.0017	0.0066 ± 0.0069	**0.0105 ± 0.0089**

Table 4.6: Relative mean errors and standard deviations for the x-, y- and z-component of the velocity for the four different methods when the motion is mainly in the y-direction

True motion in the y-direction	**z-direction**	**x-direction**	**y-direction**
BM	**1.1 % ± 1.0 %**	**1.2 % ± 0.89 %**	59.3 % ± 3.2 %
TO Jensen	2.6 % ± 1.7 %	4.5 % ± 3.1 %	16.8 % ± 5.9 %
TO 3 freq. ranges	2.6 % ± 1.7 %	6.6 % ± 6.9 %	15.4 % ± 6.3 %
TO 4 freq. ranges	2.6 % ± 1.7 %	6.6 % ± 6.9 %	**10.5 % ± 8.9 %**

4.3 Circular Motion

The 3D circular motion was used to compare the performance of the four estimators. This motion represents a more realistic motion in the sense of being three dimensional, i. e. it consists of non-zero displacements in all three directions simultaneously. In addition, the circular motion is built up of displacements of varying magnitudes. Hence, applying the motion estimators to this data set, enabled a comparison in a more realistic setting. The same point was selected to track and the same size of the ROI was chosen for all four motion estimators. Figure 4.12 displays the point selected to track in the (z, x) plane.

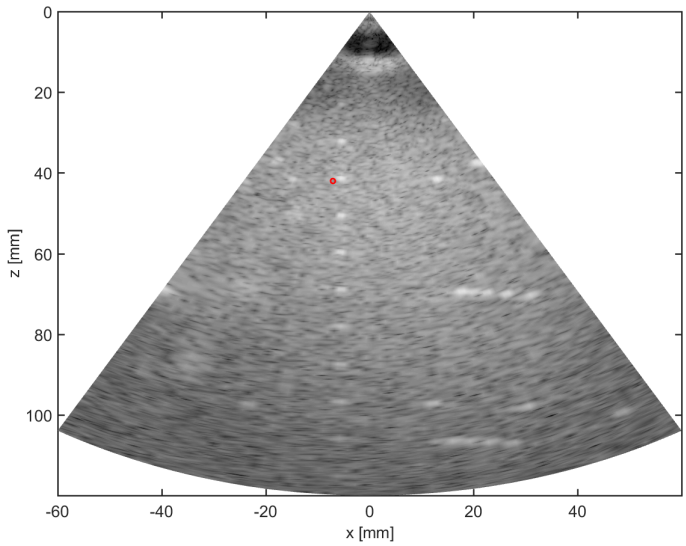

Figure 4.12: The point selected to track for the phantom experiment with circular motion, shown in the (z, x) plane.

4.3.1 Estimated Displacements

The displacements were estimated in spherical coordinates before being converted to Cartesian coordinates. The resulting Cartesian displacement curves are shown in Figure 4.13, where the black lines indicate the true motion in each direction.

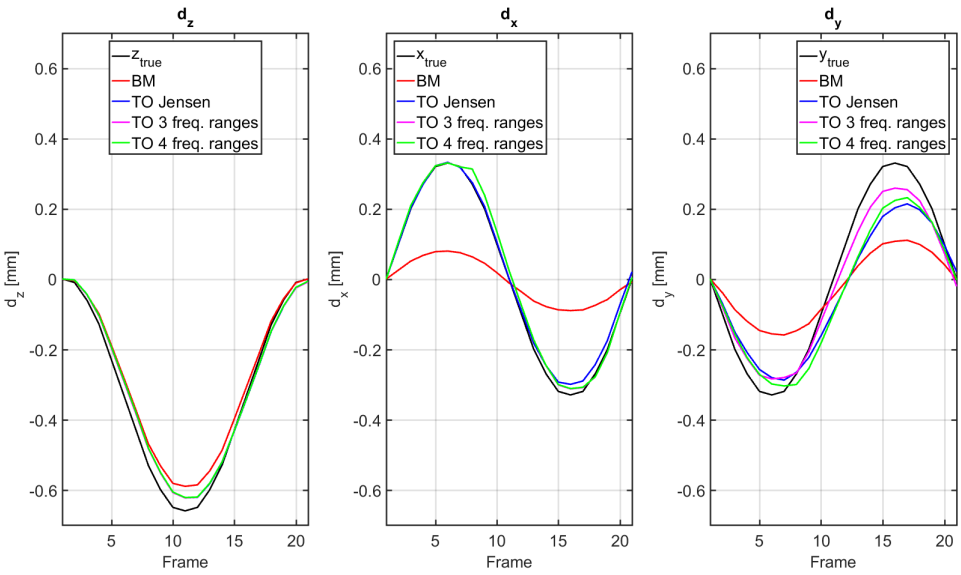

Figure 4.13: The displacement in each direction given in Cartesian coordinates for the phantom experiment with circular motion.

As can be observed from the figure, the TO methods apparently yield identical estimates of the displacement in the z-direction, while the block matching method seems to slightly underestimate the z-component of the displacement compared to the true motion. In the x-direction, the TO methods yield estimates of the displacement curve that are close to the true motion, while the block matching method seems to underestimate the motion. In the y-direction, all methods seem to underestimate the motion. However, block matching yields the most significant underestimate compared to the true motion.

4.3.2 Estimated Velocities

In order to be able to compare the motion estimation schemes without the accumulating error that is present in the displacements curves, the estimated velocities, given in Cartesian coordinates, are presented in Figure 4.14. The black lines illustrate the true velocities according to the motions introduced when carrying out the experiment.

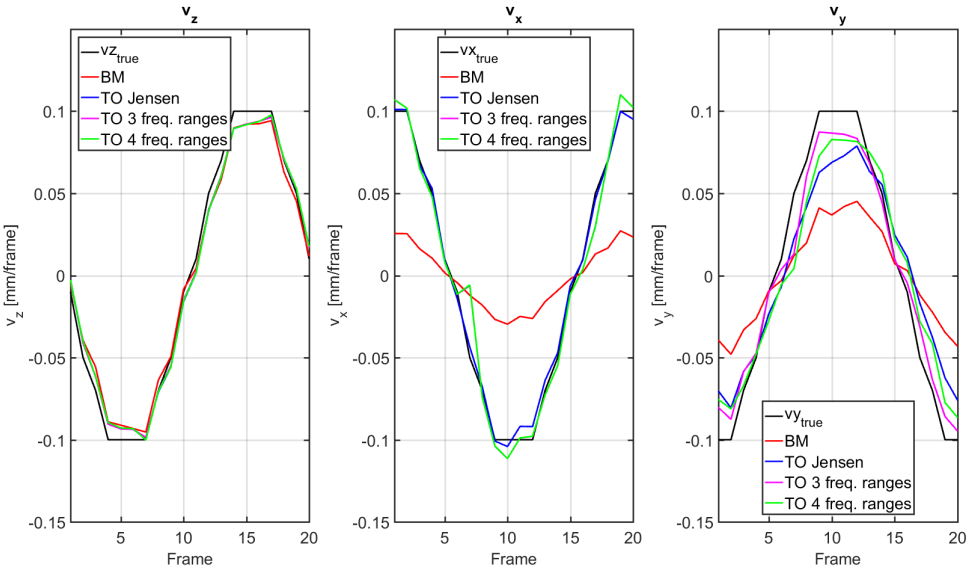

Figure 4.14: The velocity in each direction given in Cartesian coordinates for the phantom experiment with circular motion.

The figure shows that all four methods yield estimates close to the true velocity in the z-direction. According to the observations from the displacement curves, the block matching method seems to underestimate the motion significantly in both the x- and y-direction. However, the TO methods yield estimates of the x-component of the velocity close to the true motion. All four methods seem to underestimate the velocity in the y-direction.

4.3.3 Error Measurements

A quantitative comparison of the motion estimators, when applied to the 3D circular motion, is given by error measurements. Figure 4.15 gives the deviations between the estimated and the true velocity in each direction.

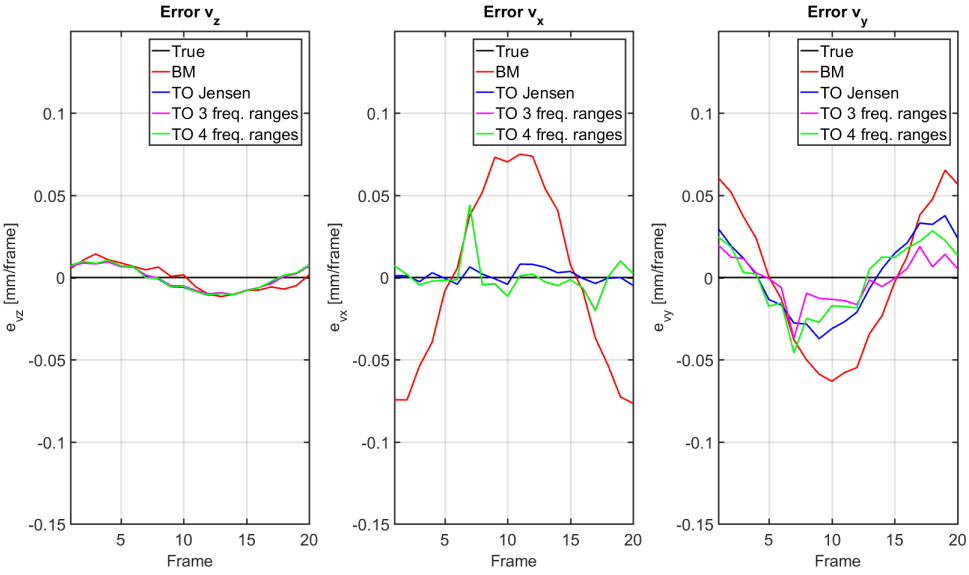

Figure 4.15: Error plot showing the deviation between the estimated velocity and the true velocity in each direction of the phantom experiment with circular motion.

From the figure it can be observed by visual inspection that the errors related to the TO methods in the z- and y-directions seem to be correlated with the corresponding velocity curves. For the block matching method, the correlation is most prominent in the x- and y-directions. The displacement and velocity curves clearly showed that the block matching method underestimated the motion. This finding is reflected in the large deviation between the velocity estimated by block matching and the true velocity.

The mean errors and standard deviations of the four methods are calculated for the 3D circle experiment and summarized in Table 4.7. The smallest mean error in each direction and the corresponding standard deviation is highlighted in bold. It can be noticed that the 3D circle motion has non-constant velocity in each direction. Therefore, the bias and variance of the estimators cannot be calculated directly from the mean errors and standard deviations in this case.

Table 4.7: Mean errors and standard deviations for the velocity in the x-, y- and z-directions for the four different methods

	z-direction	**x-direction**	**y-direction**
BM [mm/frame]	0.0071 ± 0.0036	0.0494 ± 0.0255	0.0396 ± 0.0206
TO Jensen [mm/frame]	0.0065 ± 0.0032	**0.0032 ± 0.0025**	0.0220 ± 0.0106
TO 3 freq. ranges [mm/frame]	**0.0062 ± 0.0031**	0.0067 ± 0.0099	**0.0107 ± 0.0085**
TO 4 freq. ranges [mm/frame]	0.0065 ± 0.0034	0.0067 ± 0.0100	0.0183 ± 0.0098

4.3.4 3D Plot

The estimated displacements are visualized in a 3D plot corresponding to each motion estimation method and shown in Figure 4.16. The black lines indicate the true 3D displacement curves, and serve as a reference for the estimated displacements. The estimated displacement curves are color coded according to the mean value of the displacement error in all three directions. The error is accumulating as it is based on the estimated displacements.

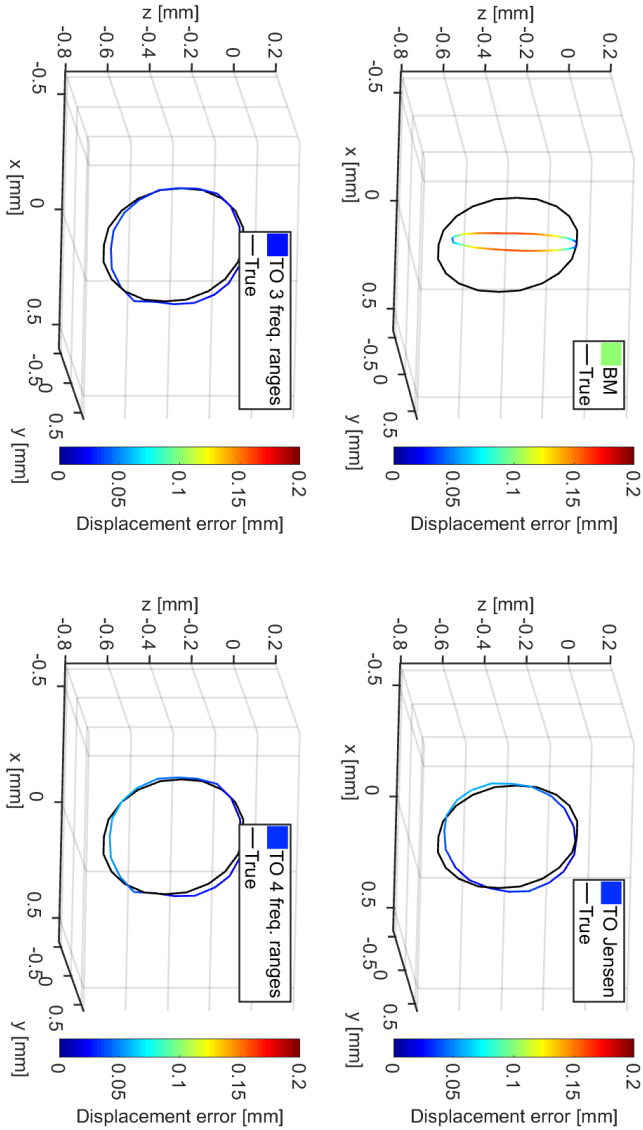

Figure 4.16: 3D plot of the estimated circular motion, color coded according to the mean displacement error.

4.4 *In Vivo* Example

The motion estimators are aimed at being able to estimate the motion of cardiac tissue. Hence, it was desirable to test the motion estimators on data from an *in vivo* example of a human heart. Since the ultrasound data was acquired from a real, human heart, the true motion is unknown. Therefore, the motion estimators can only be compared against each other. The same point in the heart wall was selected to track using all four motion estimation methods. This point is shown in Figure 4.17.

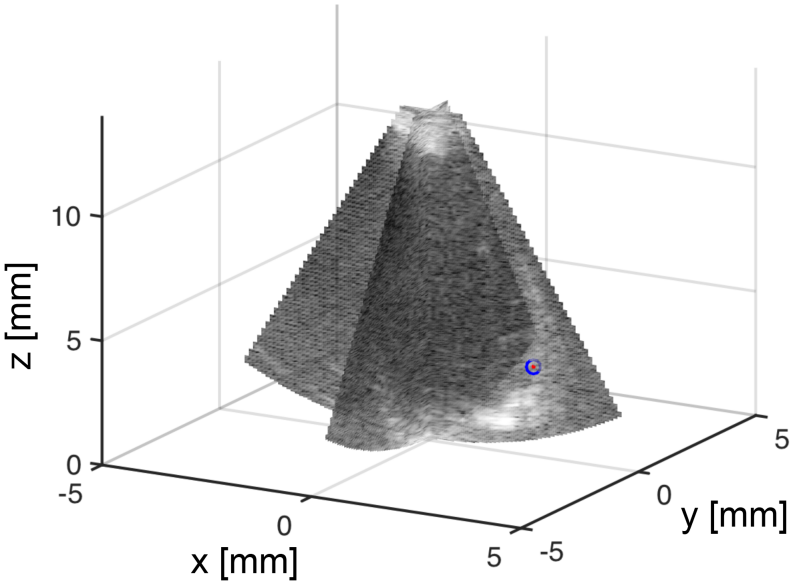

Figure 4.17: The point in the heart wall selected to track in the *in vivo* example.

Figure 4.18 shows the estimated displacements for the selected point in the heart wall in z-, x- and y-directions, resulting from all four motion estimation methods.

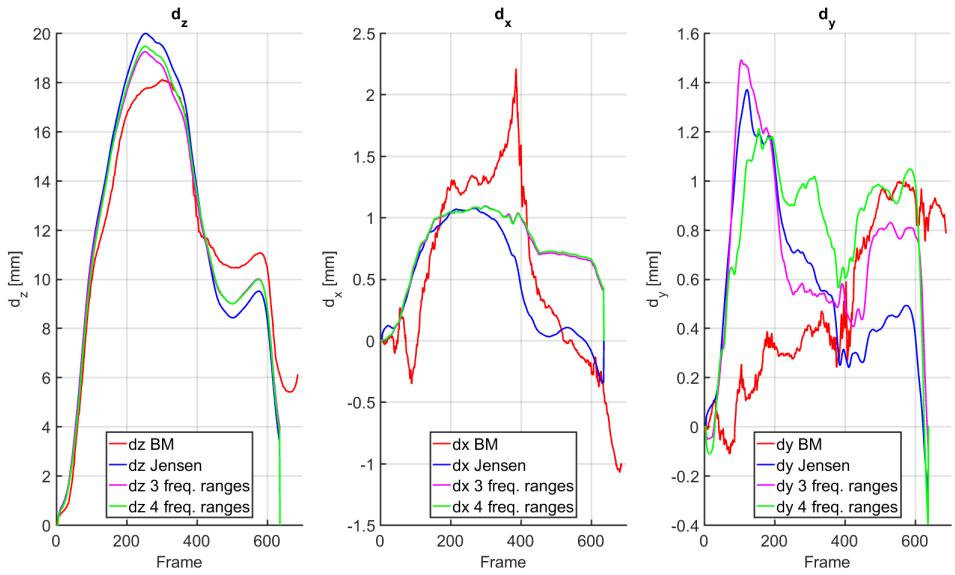

Figure 4.18: Comparison of the estimated displacements resulting from all four motion estimation methods for the *in vivo* example.

From the figure it can be observed that all four methods yield similar trajectories in the z-direction. The TO methods seem to yield similar trajectories in the x- and y-directions as well. However, the x- and y-trajectories estimated by the block matching method deviate from the trajectories estimated by the TO methods, especially in the y-direction.

Figure 4.19 shows a 3D plot of the estimated displacements for the selected point resulting from the TO method based on keeping four separate ranges of spatial frequency. The motion of the selected point is tracked through almost one full cardiac cycle. Therefore, it is expected that the point will end up close to its original position. The blue, red and green coloring indicates different periods of the cardiac cycle.

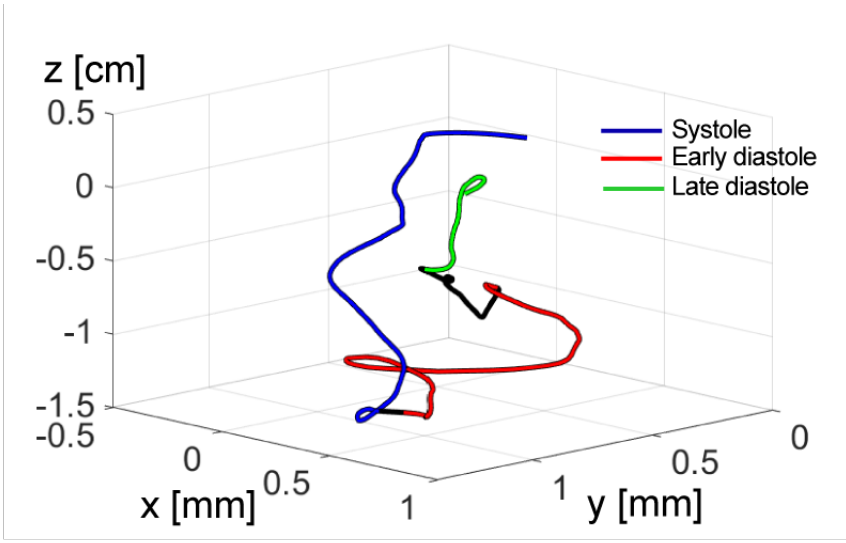

Figure 4.19: 3D plot showing the estimated displacement curve for the *in vivo* example, resulting from the motion estimation method based on keeping four separate ranges of spatial frequency.

4.5 Computational Efficiency

Table 4.8 gives the computational efficiency of the four motion estimation methods. The run times were measured for performing the motion estimation and converting from spherical to Cartesian coordinates for the sequence of 21 frames from the phantom experiment with circular motion. The run times were scaled to yield the run time per frame. In addition, the run times for 800 frames, which will be a typical number of frames for an *in vivo* acquisition of one heart cycle using ultrafast imaging, were calculated. The execution time for the block matching approach is given for tracking of one point. The procedures were run on a Windows 7 stationary computer featuring a 3.2 GHz Intel Core i5 processor and 16 GB RAM.

Table 4.8: Computational efficiency of the motion estimators

Method	**Run time per frame [s]**	**Run time for 800 frames [h]**
Block matching (for one point)	13.05	2.9
Jensen's approach	3.84	0.85
3 separate frequency ranges	3.39	0.75
4 separate frequency ranges	4.17	0.93

It is important to note that the run time for the block matching method is given for tracking one point, while the run times of the TO methods are given for calculating the velocities of all points in the image frame. The measured run times indicate that the block matching method is slower than the TO methods. The TO method based on three separate ranges of spatial frequency seems to be the fastest motion estimation algorithm.

5 Discussion

In this chapter, the results presented in the previous chapter will be discussed. Aspects such as accuracy, computational efficiency and calibration of spatial frequencies will be reviewed. In addition, suggestions for further work will be given.

Four motion estimation methods aimed at tracking the 3D motion of cardiac tissue have been implemented using Matlab. The estimators have been applied to several sets of ultrasound data featuring different types of motion in order to be able to compare the performance of the estimators. Accuracy and computational efficiency of the estimators have been considered in the comparison. Three of the estimators are based on TOs, while the fourth estimator is based on speckle tracking using block matching. The three estimators based on TOs work in the frequency domain, while the motion estimator based on speckle tracking works in the spatial domain.

5.1 Introduction of Transverse Oscillations

Three different filtering schemes have been used to produce TOs. Since oscillations are already present in the axial direction of RF images, the filtering was only applied to the azimuth and elevation directions. The first method, based on the work done by Jensen's research group, was shown to produce two double-oscillating fields. Each field features oscillations in one transverse direction in addition to the axial direction. The spatial frequency content of each double-oscillating field consists of two separate ranges of frequency. The second approach produces a 3D field featuring oscillations in both transverse directions in addition to the axial direction. This was achieved by filtering in both transverse directions simultaneously. The resulting frequency spectrum showed four separate ranges of spatial frequency. The third filtering method produced a 3D field oscillating in three transverse directions by filtering in both transverse directions simultaneously to keep only three separate ranges of spatial frequency. The second and third approach are similar in producing one single 3D field used to estimate all three velocity components.

The locations of the frequency ranges give the wavelengths of the TOs, while the widths of the frequency ranges give the bandwidths of the TOs. As the locations and widths of the frequency ranges are given by the filters, these TO parameters can easily be changed

by adjusting the filters. This is one of the main advantages of the filtering-based approach for introducing TOs over the beamforming approach. The development of the different filtering schemes have shown that the locations of the frequency ranges can easily be changed. However, it is necessary to choose the wavelengths of the TOs carefully. Close to the edges of the frequency spectrum the signal is weak, and hence placing the subapertures close to the edges will give little information about the images. Placing the subapertures close to the center of the frequency spectrum yield long wavelengths of the TOs and will therefore limit the accuracy of the estimates. Therefore, a compromise between placing the subabertures close to the edges and close to the center of the frequency spectrum must be made.

A drawback of the introduction of the TOs is the reduced spatial resolution in the transverse directions. This can be observed by studying the resulting RF images after filtering. Before filtering, the spatial resolution of the system is approximately 0.7 mm in the axial direction, and 1.5 mm and 1.8 mm in the azimuth and elevation directions, respectively, at a depth of 6 cm. After filtering the spatial frequency content using for instance the method based on keeping four separate ranges of frequency, the resolution is still approximately 0.7 mm in the axial direction, while in the azimuth direction the resolution is reduced to approximately 5 mm at a depth of 6 cm. The reduced resolution is a result of the filtering process that limits the spatial bandwidth of the images.

5.2 Linear Motion Results

In the phantom experiments with linear motion, the displacements introduced were 0.1 mm between each image frame in all directions. The block matching method seemed to underestimate the motion in both transverse directions. This can be an issue of interpolation, in addition to the resolution being poorer in the transverse directions than in the axial direction. As previously stated, the axial resolution of the system is approximately 0.7 mm. At a depth of 6 cm, which will be typical for imaging of the left ventricle, the resolution in the azimuth direction will be approximately 1.5 mm, while in the elevation direction it will be approximately 1.8 mm. Hence, a displacement of 0.1 mm is small compared to the spatial resolution of the system. In order to be able to estimate sub-pixel motion using the block matching method, the data must be interpolated. Interpolating by a factor of five in the axial direction showed to yield estimates of the z-component of the motion close to the true motion. The spatial resolution is significantly better in the axial direction than in the transverse directions. Therefore, it can be assumed that a larger interpolation factor is necessary in the transverse directions in order to obtain acceptable results. However, increasing the interpolation factor, increases the computation time significantly. The interpolation factor is therefore limited by the increase in computation time.

Another drawback of the introduced displacements being small compared to the spatial resolution of the system, is the uncertainty of such a small motion. Inaccuracy of the stepper motor and oscillations in the motion of the probe after introducing a step of the movement are possible sources of uncertainty. Therefore, it is not possible to be

certain that the introduced displacements were precisely 0.1 mm between each consecutive image frame. However, it is necessary that the motion be small, in order to be able to estimate the displacements using the TO methods. These methods are, as previously stated, limited by aliasing effects, and can only estimate displacements shorter than half the wavelength in the corresponding direction. The wavelength in the axial direction is approximately 0.6 mm, while at a depth of 6 cm the transverse wavelengths are approximately 3-4 mm. The transverse wavelengths given in mm are increasing with depth.

In order to introduce displacements purely in either x- y- or z-direction, it was necessary to ensure that the probe was perfectly aligned with the directions of motion for the stepper motor. A tilting of the probe would cause the motion introduced in one direction by the stepper motor to influence two or all three components of the motion displayed in the sequence of ultrasound images. The alignment of the probe was carried out by visual inspection and by the use of the caliper tool on the scanner. These are not accurate tools, and it is clear that this way of setting up the system introduces uncertainty regarding the true motion. This implies that the error measurements, which are based on the assumption that the true motion in each direction equals the attempted introduced motion, are questionable. In order to be able to compare the motion estimators in a setting where the true motion is fully known, a simulated data set must be provided. However, this was out of the scope of this thesis.

Figures 4.6, 4.7 and 4.8 showed that the estimated motion in the z-direction seemed to be approximately identical for all TO methods. This behavior can be explained by the fact that all three TO methods estimate the axial velocity component based on the unfiltered spatial frequency content, as in conventional TDI. The estimated axial motion influence the z-component of the estimated Cartesian displacement. In the case of tracking a point located close to the center of the image in the transverse directions, which was the case for the results presented in this thesis, the main contribution to the z-component of the motion is given by the estimated axial component.

Examining the error measurements given in Tables 4.1, 4.2, 4.3, 4.4, 4.5 and 4.6 reveal that the block matching method yielded accurate estimates of the two velocity components not in the direction of motion. However, in the direction of motion, the velocity estimated by block matching yielded large mean errors, especially in the transverse directions. This can be a consequence of the tendency of underestimation that block matching showed.

Among the TO methods, the method based on four separate ranges of spatial frequency seemed to yield the most accurate estimates of the velocity components in the direction of motion. Considering this method, the average of the relative mean errors for the three experiments with linear motion can be calculated, yielding an average relative mean error of 2.9 % in the z-direction, 10.4 % in the x-direction and 9.5 % in the y-direction. These relative mean errors can be compared to relative mean errors found in literature in order to evaluate the accuracy of the estimator. For instance in [23],

the accuracy of 3D block matching is compared to the accuracy of this TO method implemented using the special beamforming approach. The accuracy of the TO method presented in this thesis seem to perform slightly worse in the transverse directions but slightly better in the z-direction compared to the TO method considered in [23]. However, the performance of the filtering-based TO method seems to be better than the performance of block matching presented in the paper. It can be noticed that calculating the average of the relative mean errors for the TO method based on four separate ranges of spatial frequency for all experiments yielded a larger mean error of the x-component than the y-component. This is due to the large errors in the x-component of the velocity in the experiment where the true motion was mainly in the z-direction. However, the estimates are expected to be more accurate in the x-direction than in the y-direction due to the resolution being better in the azimuth direction than in the elevation direction.

5.3 Circular Motion Results

In the phantom experiment where a known 3D circular motion was introduced, the displacements vary between 0.1 mm and 0.01 mm in magnitude. The spatial resolution of the system is the same as for the phantom experiment with linear motion. Hence, these displacements are small compared to the spatial resolution. Such small displacements and the experiment setup introduce the same challenges as described in the previous section for the phantom experiment with linear motion: block matching yields underestimated motion due to the limited interpolation factor, and uncertainty regarding the true motion exists.

The error measurements related to the 3D circular motion, as displayed in Figure 4.15, show that the TO methods yield velocity estimates in the z- and y-directions that seem correlated with the true motion. This implies that the deviations between the velocity estimates and the true velocity in each direction seem to follow a similar path as the true velocity. Because of the underestimates in the transverse directions given by the block matching method, the deviations between the block matching estimates of the x- and y-components of the velocity and the true velocity components are clearly correlated with the true velocity. These systematic errors are related to the bias of the estimators. In the x-direction, the errors corresponding to the TO estimators are fluctuating about zero. According to Table 4.7, the TO method based on three separate ranges of spatial frequency yields the smallest mean errors in z- and y-directions, while the approach inspired by Jensen et al. gives the smallest mean error in the x-direction. The error measurements also show that for the TO methods, the error is larger in the y-direction than in the x-direction. This can be a consequence of the resolution being better in the azimuth direction than in the elevation direction.

5.4 *In Vivo* Results

The results from the *in vivo* example showed that the TO estimators yield similar estimates of all three motion components, as observed from Figure 4.18. The similarity is most prominent in the z- and x-directions. All TO methods use conventional TDI to estimate the axial velocity component. Therefore it is reasonable that the z-components of the estimates are similar in the three cases. As the resolution is better in the azimuth than in the elevation direction, it is expected that the estimates are more accurate in the x- than in the y-direction. The z-component of the trajectory estimated by block matching seems to be similar to the estimates given by the TO methods. As was observed in the phantom experiments, block matching yielded estimates of the motion in the z-direction close to the true motion. However, the phantom experiments also showed that the block matching method significantly underestimated the motion in the transverse directions. Therefore, it is likely that the block matching method will yield erroneous estimates of the x- and y-components of the motion in the *in vivo* example. At the same time, the TO methods showed to yield estimates of the transverse motion components close to the true motion for both phantom experiments. The TO methods are therefore more likely to yield estimates of the transverse components close to the true motion in the *in vivo* example. However, nothing can be concluded regarding the accuracy of the estimators in estimating the *in vivo* motion because the true motion is not known.

The sequence of images does not cover a full cardiac cycle. Therefore, it is not possible to compare the methods in terms of the trajectory of the selected point returning to its initial position. However, the 3D plot in Figure 4.19, showing the trajectory estimated using the TO method based on four ranges of spatial frequency, indicates that the end point of the estimated trajectory is close to the starting point.

One main difference between the phantom experiments and the *in vivo* example is that in the phantom experiments the motion is uniform throughout the entire 3D volume, while the *in vivo* motion is non-uniform. Uniform motion implies that all image points show the same motion from one image frame to the next, or in other words, the structures in the image are not deforming. In the case of deformation, points will move relative to each other. This implies for block matching that the kernel size must be reduced in order to yield accurate estimates. If the kernel is large, it is likely to include points that move relative to each other from one image frame to the next. The speckle pattern of the kernel will then change from frame to frame, and yield poorer block matching estimates. For the TO methods, motion estimation in the case of deformation require improved spatial resolution. Hence, the bandwidth of the TOs must be increased in order to yield accurate estimates. These considerations show that the kernel in the block matching method can be viewed as corresponding to the bandwidth of the TOs.

5.5 Computational Efficiency

The motion estimators were developed to compare the accuracy as a first priority. Therefore, the implementation was not optimized with respect to the execution time of the estimation procedures. However, a comparison of the computational efficiency of the estimators was performed and showed that the TO method based on three separate ranges of spatial frequency was the most efficient of the four methods. The comparison also showed that the TO methods performed quite similarly in terms of computation time. Block matching showed to be the slowest estimator, requiring a run time almost four times the run time of the fastest TO estimator. It is important to note that the TO methods estimate the velocity of each point of every image frame in the sequence of ultrasound images. The displacement or velocity of any given point can be retrieved from this information at a later point in time. The run time measurements for the TO methods give the time required to estimate the velocity maps. The block matching method is based on the selection of a point desired to track, prior to performing the motion estimation. Therefore, the run time of the block matching approach gives the time required for estimating the velocity of one single point. The block matching procedure must be repeated for each point desired to track. From the run time measurements it can therefore be concluded that the TO methods are better suited for motion estimation of multiple points than block matching.

The reason for the block matching method being the slowest estimator is likely to be related to the calculation of the SAD coefficients. Despite the SAD approach being known as the faster approach to find the best match of the kernel in the search window, the 3D search requires a high number of calculations. The computational load increases with increasing size of the search window, increasing size of the kernel and increasing interpolation factor. The reason for the TO method based on three separate ranges of spatial frequency being the fastest TO approach is likely to be related to the number of subapertures being lower than for the two other TO methods. Fewer subapertures leads to less calculations required for computation of autocorrelation functions, spatial averaging and phases of the autocorrelation functions. This will in turn yield a faster algorithm. Using three subapertures instead of four can be assumed to require 3/4 of the run time of the method using four subapertures. However, 4.17 s * 3/4 = 3.13 s, meaning that this assumption is not accurate.

Cardiologists typically use a model consisting of 18 segments for the left ventricle. Hence, being able to track one point in each segment is useful in the analysis of the left ventricular function. Tracking 18 points with speckle tracking will require 18 times as much time as the tracking of one point. For a sequence of 800 frames, this total run time will be approximately 52.5 hours, which is an excessive amount of time. Hence, in order for block matching to be useful for the cardiologists, the execution time must be significantly reduced. The computational efficiency of the block matching algorithm can be improved by reducing the size of the kernel, the search window and the interpolation factor. However, reducing these sizes will affect the accuracy of the estimator. The run times of almost one hour for the TO methods to estimate the motion of 800 frames must

also be reduced in order for the methods to be useful in clinical applications.

5.6 Calibration of Spatial Frequencies

The motion estimators based on TOs are dependent on the spatial frequencies f_r, f_θ and f_ϕ of the ultrasound images to estimate the motion. Therefore, it is necessary to provide good values for the spatial frequencies in order for the estimators to yield precise estimates of the motion. Calibration procedures were developed in order to estimate the spatial frequencies. The calibration was performed by reversing the motion estimation procedures to estimate the spatial frequencies from a known motion, instead of estimating the motion from known spatial frequencies. This implies that a calibration procedure corresponding to each motion estimation scheme was developed. The calibration of the spatial frequencies revealed a need to scale the estimated spatial frequencies in order for the motion estimators to provide estimates similar to the expected motion. It is important to note that the scaling of the estimated spatial frequencies only affects the scaling of the estimated motion, and not the shapes of the displacement or velocity curves. The need to scale the estimated spatial frequencies can be caused by a missing factor in the equations used to calculate the spatial frequencies from the known motion and the velocity from the known spatial frequencies. Another explanation can be that the true motion is in fact different from what was expected, and the estimated spatial frequencies need not be scaled. The explanation can also be a combination of the two, where each explanation holds for one or two of the components of the motion. Instead of applying calibration procedures, the theoretical values for the spatial frequencies can be calculated from the frequency spectra.

Estimating the spatial frequencies was done by choosing a ROI in the relevant image frame and introducing a motion of one pixel in each direction by creating a new image frame consisting of the ROI shifted one pixel in each direction. This procedure was repeated for each frame in the sequence of ultrasound images to calculate the spatial frequencies corresponding to each image. The temporal averages of the spatial frequencies estimated for all image frames in each direction were calculated to reduce the variance. The temporal averages of the spatial frequencies were used in the motion estimation procedures.

In the calibration procedures it was important that the introduced displacements did not exceed the limit of half the wavelength of the oscillations in each direction. If the applied displacements exceed this limit in any of the directions, aliasing effects will occur and the estimated spatial frequency in the corresponding direction will be erroneous. Therefore, it was important to be careful when choosing the displacements to be introduced. In order to facilitate displacements smaller than one pixel, interpolation can be applied. However, interpolation will increase the computational load of estimating the spatial frequencies.

5.7 Further Work

There are several aspects of the four motion estimation methods that can be improved in a future extension to this study. Further improvement of the TO methods by choosing different values for f_{0x}, f_{0y}, σ_x and σ_y can be explored. These parameters give the locations and the widths of the frequency ranges, and hence they affect the wavelengths and bandwidths of the TOs. Changing the wavelengths and bandwidths of the TOs will affect the motion estimates. The block matching method is dependent on several parameters, such as the size of the kernel, the search window and the interpolation factor. Changing the size of the kernel affects the accuracy of the block matching method, while the size of the search window determines the maximum displacement possible to detect in each direction. Interpolation enables the detection of sub-pixel motion, and is probably the most important parameter to explore regarding improving the block matching estimates.

Optimizations regarding the execution time are necessary in order to provide motion estimation tools for clinical use. Such a tool will typically be used in post-processing of ultrasound images by cardiologists, as it can provide the clinician with quantitative measurements of the motion of tissue. However, the execution time must be reduced in order to yield acceptable waiting times for the user.

A further optimization of the calibration procedures by estimating the spatial frequencies from several introduced displacements of different magnitudes, can also be explored. The mean values of the estimated spatial frequencies in each direction may offer improved estimates of the spatial frequencies.

Further work may also include the development of an application that enables the user to select the points desired to track in an ultrasound image, and visualizes the estimated motions of the selected points. Tracking several points located in the heart wall may enable the estimation of strain and strain rate of the tissue. Estimation of the stiffness of tissue can be performed by estimating the shear wave velocity. This has been described by Salles et al. in [28], and can be an interesting extension to this study.

6 | Conclusions

In this thesis, four motion estimation methods aimed at estimating the motion of cardiac tissue have been explored. Three of the estimators work in the frequency domain and use transverse oscillations to estimate the motion, while the fourth estimator uses the block matching technique of speckle tracking. The transverse oscillations are introduced by applying three different filtering schemes, one for each of the three methods. Two of these filtering schemes are based on previous work and publications, while the third is a novel approach. The four motion estimators were applied to experimental phantom data showing 1D linear motions or 3D circular motion. In addition, the estimators were tested on an *in vivo* example of the motion of a human heart. The performance of the estimators was compared in terms of accuracy and computational efficiency.

It has been shown that the motion estimators based on transverse oscillations are able to estimate the motion of a selected point at a reasonable speed compared to speckle tracking. However, the computational efficiency must be improved in order to satisfy requirements for clinical use. The speckle tracking method showed to underestimate the motion in the transverse directions of the phantom experiments, both in the case of linear and circular motion. This underestimation is likely to be caused by the small motion in the data sets, in combination with the poor resolution in the transverse directions and the limited interpolation factor. The underestimation, in combination with the poor performance in terms of computational efficiency, implies that speckle tracking might not be well-suited for motion estimation in 3D. The novel filtering approach, based on filtering the spatial frequency content of the ultrasound images to keep three separate ranges of frequency, showed to be the most accurate in estimating the z- and y-component of the velocity for the phantom experiment with circular motion. The x-component of the velocity in the phantom experiment with circular motion was most accurately estimated by the filtering approach based on the work done by Jensen's research group. For the *in vivo* example, nothing can be concluded regarding the accuracy of the estimators because the true motion is unknown. However, the three TO methods yielded similar estimates of all three components of the motion.

Bibliography

[1] Cardiovascular diseases (cvds). http://www.who.int/mediacentre/factsheets/fs317/en/, 2016. Accessed: 28.03.2017.

[2] Silent ischemia and ischemic heart disease. http://www.heart.org/HEARTORG/Conditions/HeartAttack/TreatmentofaHeartAttack/Silent-Ischemia-and-Ischemic-Heart-Disease_UCM_434092_Article.jsp#.WSBLnfmLRhE, 2016. Accessed: 20.05.2017.

[3] S. Urheim, T. Edvardsen, H. Torp, B. Angelsen, and O. A. Smiseth. Myocardial strain by doppler echocardiography. *Circulation*, 102(10):1158–1164, 2000.

[4] J. D'hooge, B. Bijnens, J. Thoen, F. Van de Werf, G. R. Sutherland, and P. Suetens. Echocardiographic strain and strain-rate imaging: a new tool to study regional myocardial function. *IEEE Transactions on Medical Imaging*, 21(9):1022–1030, 2002.

[5] C. Jia, R. Olafsson, S. w. Huang, T. J. Kolias, K. Kim, J. M. Rubin, H. Xie, and M. O'Donnell. Comparison of 2-d speckle tracking and tissue doppler imaging in an isolated rabbit heart model. *IEEE Transactions on Ultrasonics, Ferroelectrics, and Frequency Control*, 57(11):2491–2502, 2010.

[6] J. J. Heger, A. E. Weyman, L. S. Wann, J. C. Dillon, and H. Feigenbaum. Cross-sectional echocardiography in acute myocardial infarction: detection and localization of regional left ventricular asynergy. *Circulation*, 60(3):531–538, 1979.

[7] T. Edvardsen, H. Skulstad, S. Aakhus, S. Urheim, and H. Ihlen. Regional myocardial systolic function during acute myocardial ischemia assessed by strain doppler echocardiography. *Journal of the American College of Cardiology*, 37(3):726 – 730, 2001.

[8] M. Dandel, H. Lehmkuhl, C. Knosalla, N. Suramelashvili, and R. Hetzer. Strain and strain rate imaging by echocardiography-basic concepts and clinical applicability. *Current cardiology reviews*, 5(2):133–148, 2009.

[9] B. Jung, M. Markl, D. Föll, and J. Hennig. Investigating myocardial motion by mri using tissue phase mapping. *European Journal of Cardio-Thoracic Surgery*, 29(Supplement 1):150–157, 2006.

[10] L. Axel. *Noninvasive Measurement of Cardiac Strain with MRI*, pages 249–256. Springer US, 1997.

[11] W. N. McDicken, G. R. Sutherland, C .M. Moran, and L. N. Gordon. Colour doppler velocity imaging of the myocardium. *Ultrasound in Medicine & Biology*, 18(6):651 – 654, 1992.

[12] J. D'hooge, A. Heimdal, F. Jamal, T. Kukulski, B. Bijnens, F. Rademakers, L. Hatle, P. Suetens, and G. R. Sutherland. Regional strain and strain rate measurements by cardiac ultrasound: principles, implementation and limitations. *European Heart Journal-Cardiovascular Imaging*, 1(3):154–170, 2000.

[13] P. R. Hoskins, K. Martin, and A. Thrush. *Diagnostic Ultrasound: Physics and Equipment*, volume 2. Cambridge University Press, 2010.

[14] R. W. Cootney. Ultrasound imaging: principles and applications in rodent research. *Ilar Journal*, 42(3):233–247, 2001.

[15] R. W. Gill. Measurement of blood flow by ultrasound: Accuracy and sources of error. *Ultrasound in Medicine and Biology*, 11(4):625–641, 1985.

[16] B. S. Garra. Imaging and estimation of tissue elasticity by ultrasound. *Ultrasound Quarterly*, 23(4):255–268, 2007.

[17] O. T. vonRamm and F. L. Thurstone. Cardiac imaging using a phased array ultrasound system. i. system design. *Circulation*, 53(2):258—262, 1976.

[18] T. H. Marwick, C.-M. Yu, and J. P. Sun. *Myocardial Imaging: Tissue Doppler and Speckle Tracking*, volume 1. Blackwell Futura, 2007.

[19] J. Meunier, M. Bertrand, G. E. Mailloux, and R. Petitclerc. Local myocardial deformation computed from speckle motion. In *Proceedings. Computers in Cardiology 1988*, pages 133–136, 1988.

[20] J. Meunier. Tissue motion assessment from 3d echographic speckle tracking. *Physics in Medicine and Biology*, 43(5):1241, 1998.

[21] B. Dunmire, K.W. Beach, K-H Labs, M. Plett, and D.E. Strandness Jr. Cross-beam vector doppler ultrasound for angle-independent velocity measurements. *Ultrasound in Medicine & Biology*, 26(8):1213 – 1235, 2000.

[22] M. D. Fox and W. M. Gardiner. Three-dimensional doppler velocimetry of flow jets. *IEEE Transactions on Biomedical Engineering*, 35(10):834–841, 1988.

[23] S. Salles, H. Liebgott, D. Garcia, and D. Vray. Full 3-d transverse oscillations: a method for tissue motion estimation. *IEEE Transactions on Ultrasonics, Ferroelectrics, and Frequency Control*, 62(8):1473–1485, 2015.

[24] S. Bech, S. Salles, and H. Torp. 2d motion estimation using high frame rate ultrasound imaging and transverse oscillations: A python implementation, 2016.

[25] J. A. Jensen and P. Munk. A new method for estimation of velocity vectors. *IEEE Transactions on Ultrasonics, Ferroelectrics, and Frequency*, 43(3):837–851, 1998.

[26] M. E. Anderson. Multi-dimensional velocity estimation with ultrasound using spatial quadrature. *IEEE transactions on ultrasonics, ferroelectrics, and frequency control*, 45(3):852–861, 1998.

[27] F. Varray and H. Liebgott. An alternative method to classical beamforming for transverse oscillation images: Application to elastography. In *2013 IEEE 10th International Symposium on Biomedical Imaging*, pages 716–719, 2013.

[28] S. Salles, A. J. Y. Chee, D. Garcia, A. C. H. Yu, D. Vray, and H. Liebgott. 2-d arterial wall motion imaging using ultrafast ultrasound and transverse oscillations. *IEEE Transactions on Ultrasonics, Ferroelectrics, and Frequency Control*, 62(6):1047–1058, 2015.

[29] M. J. Pihl and J. A. Jensen. 3d vector velocity estimation using a 2d phased array. In *2011 IEEE International Ultrasonics Symposium*, pages 430–433, 2011.

[30] M. J. Pihl and J. A. Jensen. Measuring 3d velocity vectors using the transverse oscillation method. In *2012 IEEE International Ultrasonics Symposium*, pages 1881–1885, 2012.

[31] C. VanPutte, J. Regan, and A. Russo. *Seeley's Essentials of Anatomy & Physiology*. McGraw-Hill Education, 2016.

[32] D. H. MacIver. The relative impact of circumferential and longitudinal shortening on left ventricular ejection fraction and stroke volume. *Experimental & Clinical Cardiology*, 17(1):5–11, 2012.

[33] S. Langeland, J. D'hooge, H. Torp, B. Bijnens, and P. Suetens. Comparison of time-domain displacement estimators for two-dimensional {RF} tracking. *Ultrasound in Medicine & Biology*, 29(8):1177 – 1186, 2003.

[34] G. R. Sutherland, G. Di Salvo, P. Claus, J. D'hooge, and B. Bijnens. Strain and strain rate imaging: a new clinical approach to quantifying regional myocardial function. *Journal of the American Society of Echocardiography*, 17(7):788–802, 2004.

[35] F. Weidemann, F. Jamal, G. R. Sutherland, P. Claus, M. Kowalski, L. Hatle, I. De Scheerder, B. Bijnens, and F. E. Rademakers. Myocardial function defined by strain rate and strain during alterations in inotropic states and heart rate. *American Journal of Physiology - Heart and Circulatory Physiology*, 283(2):H792–H799, 2002.

[36] H. Yamada, T. Oki, T. Tabata, A. Iuchi, and S. Ito. Assessment of left ventricular systolic wall motion velocity with pulsed tissue doppler imaging: Comparison with peak dp/dt of the left ventricular pressure curve. *Journal of the American Society of Echocardiography*, 11(5):442 – 449, 1998.

[37] I.Mirsky and W. W. Parmley. Assessment of passive elastic stiffness for isolated heart muscle and the intact heart. *Circulation Research*, 33(2):233–243, 1973.

[38] G. Mundigler and M. Zehetgruber. Tissue doppler imaging: Myocardial velocities and strain - are there clinical applications? *Journal of Clinical and Basic Cardiology*, 5(2):125–132, 2002.

[39] S. Holm. Medisinsk ultralydavbildning. *Fra Fysikkens Verden*, 1, 1999 (Updated 2008).

[40] K. Baba. Development of 3d ultrasound. *Donald School Journal of Ultrasound in Obstetrics and Gynecology*, 4(3):205–215, 2010.

[41] A. Fenster, D. B. Downey, and H. N. Cardinal. Three-dimensional ultrasound imaging. *Physics in Medicine and Biology*, 46(5):R67, 2001.

[42] B. Savord and R. Solomon. Fully sampled matrix transducer for real time 3d ultrasonic imaging. In *IEEE Symposium on Ultrasonics, 2003*, volume 1, pages 945–953 Vol.1, 2003.

[43] R. S. Lazebnik and T. S. Desser. Clinical 3d ultrasound imaging: beyond obstetrical applications. Diagnostic Imaging: Continuing Medical Education, 2007.

[44] J. Bercoff. Ultrafast ultrasound imaging. In I. V. Minin and O. V. Minin, editors, *Ultrasound Imaging - Medical Applications*, chapter 01. InTech, Rijeka, 2011.

[45] Y. Liu, J. T. Frans, et al. *Cardiovascular Imaging*. CRC Press, 2009.

[46] M. Cikes, L. Tong, G. R. Sutherland, and J. D'hooge. Ultrafast cardiac ultrasound imaging: Technical principles, applications, and clinical benefits. *The Journal of the American College of Cardiology*, 7(8):812–823, 2014.

[47] L. Tong, J. Hamilton, R. Jasaityte, M. Cikes, G. Sutherland, and J. D'hooge. Plane wave imaging for cardiac motion estimation at high temporal resolution: A feasibility study in-vivo. In *2012 IEEE International Ultrasonics Symposium*, pages 228–231, 2012.

[48] B. F. Osmanski, M. Pernot, G. Montaldo, A. Bel, E. Messas, and M. Tanter. Ultrafast doppler imaging of blood flow dynamics in the myocardium. *IEEE Transactions on Medical Imaging*, 31(8):1661–1668, 2012.

[49] J. A. Jensen, O. Holm, L. J. Jensen, H. Bendsen, S. I. Nikolov, B. G. Tomov, P. Munk, M. Hansen, K. Salomonsen, K. Gormsen, J. Hansen, H. M. Pedersen, and K. Gammelmark. Ultrasound research scanner for real-time synthetic aperture data acquisition. *IEEE Transactions on Ultrasonics, Ferroelectrics and Frequency Control*, 52(5):881–891, 2005.

[50] J. A. Jensen, S. I. Nikolov, K. L. Gammelmark, and M. H. Pedersen. Synthetic aperture ultrasound imaging. *Ultrasonics*, 44(Supplement):e5–e15, 2006.

[51] G. Montaldo, M. Tanter, J. Bercoff, N. Benech, and M. Fink. Coherent plane-wave compounding for very high frame rate ultrasonography and transient elastography. *IEEE Transactions on Ultrasonics, Ferroelectrics, and Frequency Control*, 56(3):489–506, 2009.

[52] P. Kruizinga, F. Mastik, N. de Jong, A. F. W. van der Steen, and G. van Soest. Plane-wave ultrasound beamforming using a nonuniform fast fourier transform. *IEEE Transactions on Ultrasonics, Ferroelectrics, and Frequency Control*, 59(12):2684–2691, 2012.

[53] J.-Y. Lu. 2d and 3d high frame rate imaging with limited diffraction beams. *IEEE Transactions on Ultrasonics, Ferroelectrics, and Frequency Control*, 44(4):839–856, 1997.

[54] T. Yoshida, M. Mori, Y. Nimura, G. Hikita, S. Takagishi, K. Nakanishi, and S. Satomura. Analysis of heart motion with ultrasonic doppler method and its clinical application. *American Heart Journal*, 61(1):61 – 75, 1961.

[55] J. B. Kostis, E. Mavrogeorgis, A. Slater, and S. Bellet. Use of a range-gated, pulsed ultrasonic doppler technique for continuous measurement of velocity of the posterior heart wall*. *Chest*, 62(5):597–604, 1972.

[56] K. Isaaz, A. Thompson, G. Ethevenot, J. L. Cloez, B. Brembilla, and C. Pernot. Doppler echocardiographic measurement of low velocity motion of the left ventricular posterior wall. *The American Journal of Cardiology*, 64(1):66 – 75, 1989.

[57] N. Yamazaki, Y. Mine, A. Sano, M. Hirama, K. Miyatake, M. Yamagishi, and N. Tanaka. Analysis of ventricular wall motion using color-coded tissue doppler imaging system. *Japanese Journal of Applied Physics*, 33(5S):3141, 1994.

[58] G. R. Sutherland, M. J. Stewart, K. W. E. Groundstroem, C. M. Moran, A. Fleming, F. J. Guell-Peris, R. A. Riemersma, L. N. Fenn, K. A. A. Fox, and W. N. McDicken. Color doppler myocardial imaging: A new technique for the assessment of myocardial function. *Journal of the American Society of Echocardiography*, 7(5):441 – 458, 1994.

[59] D. H. Evans, J. A. Jensen, and M. B. Nielsen . Ultrasonic colour doppler imaging. *Interface Focus*, 1(4):490–502, 2011.

[60] M. Wilson. The physics of diagnostic ultrasound. http://slideplayer.com/slide/4383886/. Accessed: 08.12.2016.

[61] C. Storaa, P. Åberg, B. Lind, and L.-Å. Brodin. Effect of angular error on tissue doppler velocities and strain. *Echocardiography*, 20(7):581–587, 2003.

[62] G. E. Trahey, J. W. Allison, and O. T. von Ramm. Angle independent ultrasonic detection of blood flow. *IEEE Transactions on Biomedical Engineering*, BME-34(12):965–967, 1987.

[63] L. Pérez de Isla, D. Vivas, and J. Zamorano. Three-dimensional speckle tracking. *Current Cardiovascular Imaging Reports*, 1(1):25–29, 2008.

[64] G. E. Trahey, S. M. Hubbard, and O. T. von Ramm. Angle independent ultrasonic blood flow detection by frame-to-frame correlation of b-mode images. *Ultrasonics*, 26(5):271—276, 1988.

[65] A. Opdahl, T. Helle-Valle, H. Skulstad, and O. A. Smiseth. Strain, strain rate, torsion, and twist: Echocardiographic evaluation. *Current Cardiology Reports*, 17(3):15, 2015.

[66] F. Viola and W. F. Walker. Comparison of time delay estimators in medical ultrasound. In *2001 IEEE Ultrasonics Symposium. Proceedings. An International Symposium (Cat. No.01CH37263)*, volume 2, pages 1485–1488 vol.2, 2001.

[67] A. J. H. Hii, C. E. Hann, J. G. Chase, and E. E. W. Van Houten. Fast normalized cross correlation for motion tracking using basis functions. *Computer Methods and Programs in Biomedicine*, 82(2):144 – 156, 2006.

[68] I. E. G. Richardson. *H.264 and MPEG-4 Video Compression: Video Coding for Next-generation Multimedia*. Wiley, 2003.

[69] M. Wigen and L. Løvstakken. In vivo three-dimensional intra-cardiac vector flow imaging using a 2d matrix array transducer. In *2016 IEEE International Ultrasonics Symposium (IUS)*, pages 1–4, 2016.

[70] M. D. Fox. Multiple crossed-beam ultrasound doppler velocimetry. *IEEE Transactions on Sonics and Ultrasonics*, 25(5):281–286, 1978.

[71] E. Papadofrangakis, W. E. Engeler, and J. A. Fakiris. Measurement of true blood velocity by an ultrasound system, 1981.

[72] A. L. Hall and R. B. Bernardi. Method for detecting two-dimensional flow for ultrasound color flow imaging, 1995.

[73] P. J. Phillips, A. P. Kadi, and O. T. von Ramm. Feasibility study for a two-dimensional diagnostic ultrasound velocity mapping system. *Ultrasound in medicine & biology*, 21(2):217–229, 1995.

[74] A. Brahme. *Comprehensive Biomedical Physics*. Elsevier, 2014.

[75] J. W. Goodman. *Introduction to Fourier Optics*. Roberts & Company Publishers, 2005.

[76] M. Lenge, A. Ramalli, A. Cellai, P. Tortoli, C. Cachard, and H. Liebgott. A new method for 2d-vector blood flow imaging based on unconventional beamforming techniques. In *2014 IEEE International Conference on Acoustics, Speech and Signal Processing (ICASSP)*, pages 5125–5129, 2014.

[77] H. Liebgott, A. B. Salem, A. Basarab, H. Gao, P. Claus, J. D'hooge, P. Delachartre, and D. Friboulet. Tangential sound field oscillations for 2d motion estimation in echocardiography. In *2009 IEEE International Ultrasonics Symposium*, pages 498–501, 2009.

[78] A. Basarab, P. Gueth, H. Liebgott, and P. Delachartre. Phase-based block matching applied to motion estimation with unconventional beamforming strategies. *IEEE Transactions on Ultrasonics, Ferroelectrics, and Frequency Control*, 56(5):945–957, 2009.

[79] S. L. Hahn. Multidimensional complex signals with single-orthant spectra. *Proceedings of the IEEE*, 80(8):1287–1300, 1992.

[80] X. Lai, H. Torp, and K. Kristoffersen. An extended autocorrelation method for estimation of blood velocity. *IEEE Transactions on Ultrasonics, Ferroelectrics, and Frequency Control*, 44(6):1332–1342, 1997.

[81] C. Kasai, K. Namekawa, A. Koyano, and R. Omoto. Real-time two-dimensional blood flow imaging using an autocorrelation technique. *IEEE Transactions on Sonics and Ultrasonics*, SU-32(3):458–464, 1985.

[82] S. Langeland, J. D'hooge, H. Torp, B. Bijnens, and P. Suetens. Comparison of time-domain displacement estimators for two-dimensional {RF} tracking. *Ultrasound in Medicine & Biology*, 29(8):1177 – 1186, 2003.

[83] D. H. Evans, J. A. Jensen, and M. B. Nielsen. Ultrasonic colour doppler imaging. *Interface Focus*, 1(4):490–502, 2011.

[84] H. Nobach and M. Honkanen. Two-dimensional gaussian regression for sub-pixel displacement estimation in particle image velocimetry or particle position estimation in particle tracking velocimetry. *Experiments in fluids*, 38(4):511–515, 2005.

[85] S. Li, J. M. R. S. Tavares, et al. *Shape Analysis in Medical Image Analysis*. Springer, 2014.

[86] G. Stetten. Real time 3d (rt3d) ultrasound. http://www.stetten.com/george/rt3d/. Accessed: 06.06.2017.

A Relevant Source Code

A.1 3D Filtering Methods

A.1.1 Jensen's Approach

```
[Nr, Nb, Np, Nt]=size(iq);
f0 = 0.8;
sigma = 0.0035;

%% Create filters
x=linspace(0,1,Nb);
f0x=f0;
sigmax=sigma;
upperAperture=exp(-(x-f0x).^2/(2*sigmax));
lowerAperture =fliplr(upperAperture);
lowerAperture_mask=repmat(lowerAperture,[Nr,1,Np,Nt]);
upperAperture_mask=repmat(upperAperture,[Nr,1,Np,Nt]);

y = linspace(0,1,Np);
f0y=f0;
sigmay=sigma;
leftAperture=exp(-(y-f0y).^2/(2*sigmay));
rightAperture=fliplr(leftAperture);
rightAperture_mask=repmat(rightAperture,[Nr,1,Nb,Nt]);
leftAperture_mask=repmat(leftAperture,[Nr,1,Nb,Nt]);

rightAperture_mask=permute(rightAperture_mask, [1 3 2 4]);
leftAperture_mask=permute(leftAperture_mask, [1 3 2 4]);

%% Create subapertures
IQ=fft(iq, [], 2);
iqLower=ifft(IQ.*lowerAperture_mask,[],2);
iqUpper=ifft(IQ.*upperAperture_mask,[],2);

IQ=fft(iq, [], 3);
iqRight=ifft(IQ.*rightAperture_mask,[],3);
iqLeft=ifft(IQ.*leftAperture_mask,[],3);
```

A.1.2 Four Separate Ranges of Frequency

```
[Nr, Nb, Np, Nt]=size(iq);
f0 = 0.8;
sigma = 0.0035;

%% Create filters
x=linspace(0,1,Nb);
f0x=f0;
sigmax=sigma;
upperAperture=exp(-(x-f0x).^2/(2*sigmax));
lowerAperture =fliplr(upperAperture);
lowerAperture_mask=repmat(lowerAperture,[Nr,1,Np,Nt]);
upperAperture_mask=repmat(upperAperture,[Nr,1,Np,Nt]);

y = linspace(0,1,Np);
f0y=f0;
sigmay=sigma;
leftAperture=exp(-(y-f0y).^2/(2*sigmay));
rightAperture=fliplr(leftAperture);
rightAperture_mask=repmat(rightAperture,[Nr,1,Nb,Nt]);
leftAperture_mask=repmat(leftAperture,[Nr,1,Nb,Nt]);

rightAperture_mask=permute(rightAperture_mask, [1 3 2 4]);
leftAperture_mask=permute(leftAperture_mask, [1 3 2 4]);

%% Create subapertures
IQ=fft(iq, [], 3);

iqLeft=ifft(IQ.*leftAperture_mask,[],3);
iqRight=ifft(IQ.*rightAperture_mask,[],3);
IQLEFT=fft(iqLeft, [], 2);
IQRIGHT=fft(iqRight, [], 2);

iqLowerLeft=ifft(IQLEFT.*lowerAperture_mask,[],2);
iqUpperLeft=ifft(IQLEFT.*upperAperture_mask,[],2);
iqLowerRight=ifft(IQRIGHT.*lowerAperture_mask,[],2);
iqUpperRight=ifft(IQRIGHT.*upperAperture_mask,[],2);
```

A.1.3 Three Separate Ranges of Frequency

```
[Nr, Nb, Np, Nt]=size(iq);
f0 = 0.8;
sigma = 0.0035;

%% Create filters
x=linspace(0,1,Nb);
f0x=f0;
sigmax=sigma;
upperAperture=exp(-(x-f0x).^2/(2*sigmax));
lowerAperture =fliplr(upperAperture);
lowerAperture_mask=repmat(lowerAperture,[Nr,1,Np,Nt]);
upperAperture_mask=repmat(upperAperture,[Nr,1,Np,Nt]);

y = linspace(0,1,Np);
f0y=f0;
sigmay=sigma;
leftAperture=exp(-(y-f0y).^2/(2*sigmay));
rightAperture=fliplr(leftAperture);
rightAperture_mask=repmat(rightAperture,[Nr,1,Nb,Nt]);
leftAperture_mask=repmat(leftAperture,[Nr,1,Nb,Nt]);

rightAperture_mask=permute(rightAperture_mask, [1 3 2 4]);
leftAperture_mask=permute(leftAperture_mask, [1 3 2 4]);

f01=0;
f02=1;
sigmay=sigma;
middleAperture=exp(-(y-f01).^2/(2*sigmay))+exp(-(y-f02).^2/(2*sigmay));
middleAperture_mask=repmat(middleAperture,[Nr,1,Nb,Nt]);

middleAperture_mask=permute(middleAperture_mask, [1 3 2 4]);

%% Create subapertures
IQ=fft(iq, [], 2);
iqUpper=ifft(IQ.*upperAperture_mask,[],2);
iqLower=ifft(IQ.*lowerAperture_mask,[],2);
IQUPPER=fft(iqUpper, [], 3);
IQLOWER=fft(iqLower, [], 3);

iqUpperLeft=ifft(IQUPPER.*leftAperture_mask,[],3);
iqUpperRight=ifft(IQUPPER.*rightAperture_mask,[],3);
iqLowerMiddle=ifft(IQLOWER.*middleAperture_mask,[],3);
```

B | Abstract Submitted for the IUS 2017 Conference

The abstract was accepted for oral presentation at the IUS 2017 conference.

Submission ID: 1242
Subject Classification: MEL Elastography
Presentation Preference: Oral
Student Paper: No **Participate in the Student Paper Competition**: No
Invited Speaker: No
Keywords: 3D transverse oscillations, 3D phase-based motion estimation, High frame rate imaging

Comparison of 3D tissue motion estimation methods using transverse oscillations

Solveig Bech[1], Sebastien Salles[2], Hans Torp[2]
[1]Norwegian University of Science and Technology, Trondheim, Norway, [2]Department of Circulation and Medical Imaging, Norwegian University of Science and Technology, Norway

Background, Motivation and Objective

Cardiovascular diseases are the leading cause of death globally. Such diseases may affect the left ventricular function, which in turn is closely related to the left ventricular stiffness. Estimation of cardiac deformation can give information on the myocardial stiffness, and may therefore be important in assessment of cardiovascular diseases. A 3D motion estimation scheme is necessary to measure the full cardiac motion. To do so, the use of transverse oscillations (TOs), to compute the azimuth and elevation velocity components, has been proposed. The objective of this study was to compare three different ways of introducing 3D TOs, in order to find the method best suited for cardiac motion estimation.

Statement of Contribution/Methods

The three methods use different spatial filters (Figures a-c) to filter the frequency content in order to generate TOs. A phase-based motion estimation scheme is used to estimate the 3D motion by calculating the phase of the autocorrelation after filtering and combining the phase vectors according to the method used to achieve the true velocity components.

Two experiments were performed using a locally modified, university-owned Vivid E95 scanner and a 4V probe. A tissue-mimicking phantom was conventionally scanned using a stepper motor to introduce a known 3D trajectory, and the left ventricle of one healthy volunteer was scanned using 3D high frame rate imaging (820 FPS).

Results

Figures a-c show the three filtering techniques used to introduce TOs. Figures d-f show the tracking of a known 3D circle using the three methods. The color of the estimated trajectories gives the mean error of the displacement in relation to the known trajectory. Method b yielded the best result in x-direction with mean error of 0.0204 +/- 0.0174 mm. Methods b and c gave the best results in y-direction with mean errors of 0.0344 +/- 0.0415 mm and 0.0344 +/- 0.0336 mm respectively. Method a yielded the best result in z-direction with mean error of 0.0053 +/- 0.0037 mm. Spatial filtering was used to achieve TOs, hence in all three cases it is possible to apply conventional tissue Doppler, using the entire frequency content, to estimate the motion in z-direction. The TO parameters were chosen independently for each method to yield the best result possible in each case. As method b gave the best result estimating the 3D circle, it was tested on in-vivo data as shown in Figure g.

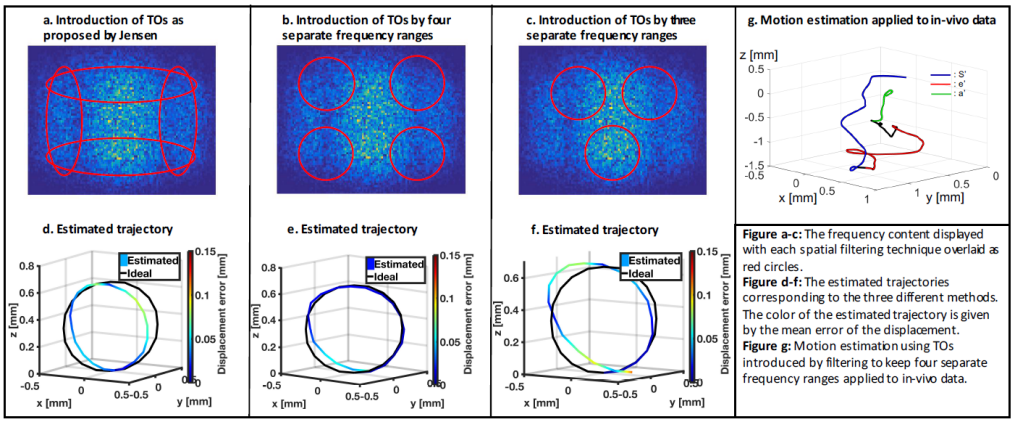

Figure a-c: The frequency content displayed with each spatial filtering technique overlaid as red circles.
Figure d-f: The estimated trajectories corresponding to the three different methods. The color of the estimated trajectory is given by the mean error of the displacement.
Figure g: Motion estimation using TOs introduced by filtering to keep four separate frequency ranges applied to in-vivo data.